J. Mat. NanoSci. 2014, 1(1), 12-30 Review

Journal of
Materials NanoScience

The impact of central metal ions in Porphyrin functionalized ZnO/TiO_2 for enhanced solar energy conversion

Samim Sardar, Prasenjit Kar and Samir Kumar Pal*

Department of Chemical, Biological and Macromolecular Sciences, S. N. Bose National Centre for Basic Sciences, Block JD, Sector III, SaltLake City, Kolkata 700 098, India

Received Date: 10th July, 2014

ABSTRACT

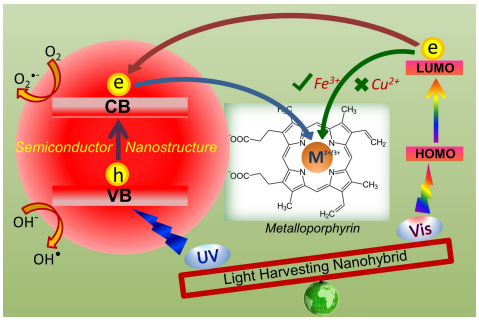

The photochemistry of porphyrins and metalloporphyrins has drawn immense research interest because of their diverse catalytic activity and biological relevance. Porphyrin sensitized devices for efficient visible light photocatalysis (VLP) and dye sensitized solar cells (DSSC) are emerging as green alternate to ruthenium dye based devices. In this review, we provide an overview of the ultrafast dynamics and role of metal ions in electron transfer processes in porphyrin sensitized devices. We have discussed some of our relevant works on biologically important organic pigments, Hematoporphyrin (HP) and Protoporphyrin IX (PP) as photosensitizer to the solar devices. Our study on HP functionalized ZnO nanorod (NR) arrays shows efficient electron migration from photoexcited HP to the host ZnO NRs leading to successful realization of twin applications of HP-ZnO nanohybrids in efficient VLP and DSSC. Another study reveals the role of iron ion and its oxidation states in electron transfer processes in HP functionalized titania. From the practical application point of view, use of porphyrin-based photocatalytic devices for water decontamination is very important, given the fact that water from natural resources contains metal ions (Fe^{3+} and Cu^{2+} especially). We have synthesized and characterized a PP-ZnO nanohybrid for a flow-type photocatalytic solar device for a prototype water decontamination plant using visible light. We explored the role of metal ions, specifically, iron (III) and copper (II) in the test water with a model contaminant, methylene blue (MB) and rationalized our observations from femtosecond to picosecond resolved electronic spectroscopic studies.

Keywords: Light-Harvesting Nanohybrids, Metalloporphyrins, Photoinduced Electron Transfer, UV and Visible-light Photocatalysis, Porphyrin-Sensitized Solar Cell, Reactive oxygen species (ROS), femtosecond transient absorption spectroscopy.

Corresponding Author: Prof. Samir Kumar Pal
Tel: +91 033 2335 5706-08
Email: skpal@bose.res.in

Cite as: *J. Mat. NanoSci., 2014, 1(1), 12-30.*

INTRODUCTION

In recent times, a significant effort has been devoted for the construction and development of artificial solar energy harvesting systems that have the ability to absorb sunlight and convert it to useful and storable forms. During photosynthesis, plants store solar energy in the form of chemical energy and the conversion of solar energy to chemical energy involves the transfer of electrons in porphyrin based chlorophyll chromophores embedded in the thylakoid membranes of chloroplast.[1] To clarify the complex

mechanism of photosynthesis, the photochemistry of porphyrins and their metal complexes has long been an interesting subject of investigation.[2-6] The complexity of electron transfer reactions in nature has led researchers to build up simplified model systems to understand the essential steps of enzyme mechanism in living organism.[7-9] The increasing demand for the complete photocatalytic mineralization of organic pollutants in water into harmless products through redox reactions necessitates the exploration of efficient catalysts able to mimic natural enzymatic systems.

Porphyrins anchored on nanocrystalline TiO_2/ZnO offer a number of advantages due to its isolation on a solid support: enhancement of its reactivity, inhibition of degradative intermolecular self-reactions and mimicking the proteic environment of the hemeprotein. Colloidal wideband gap semiconductor suspensions have been reported extensively for environmental remediation under ultraviolet band light irradiation.[10-12] Bandgap excitations in TiO_2/ZnO occur only at wavelengths less than 380 nm, which prevents it from being a potential visible light harvester. The popular photocatalyst TiO_2/ZnO can only utilize about 4% of the incoming solar energy. Therefore, a visible-light activated catalyst is desired that can take the benefit of utilizing a superior portion of the solar spectrum and would be much more effective in ecological clean-up. In the view point of effective utilization of visible solar radiation, efforts have been made to trigger a photocatalyst under visible-light by extending its photo response to the visible region by metal-ion doping,[13] nonmetal doping,[14,15] noble metal deposition,[16] narrow band-gap semiconductors coupling,[17-19] conducting polymer sensitization[20] and dye sensitization[21-23]. In the latter approach, the excited dye molecule transfers an electron into the conduction band of the semiconductor, leading to the formation of a cationic radical of the dye. The injected electron then reacts with the dioxygen adsorbed on the surface of the metal oxide (MO), and generates active species involved in the process such as $O_2^{\bullet-}$, $dye^{\bullet+}$, as shown below:

$$dye + h\upsilon \rightarrow dye^*$$

$$dye^* + MO \rightarrow dye^{\bullet+} + MO(e_{CB}^-)$$

$$MO(e_{CB}^-) + O_2 \rightarrow MO + O_2^{\bullet-}$$

$$dye^{\bullet+}, O_2^{\bullet-} + R \rightarrow Product$$

The subsequent radical chain reactions lead to the degradation and mineralization of a contaminant (R) and concurrently water in the media acts as an electron donor to regenerate the sensitizer dye.[23] For example, Zhao et al. has demonstrated a dye sensitization system incorporating $Pt(dcbpy)Cl_2$ (dcbpy = 4,4′-dicarboxy-2,2′-bipyridine) on titania for the visible-light degradation of aqueous organic pollutant 4-chlorophenol in the presence of dioxygen.[21] Sensitization of wide band gap semiconductor by organic dyes for all kinds of solar devices is unavoidable.[24,25] Design of low cost and environmentally friendly 'green' dye sensitized solar light harvesting devices relies on the nature of the organic dyes used as light-absorber materials. A considerable research effort in this direction stems from the desire to tackle a number of problems including cost and environment-compatibility.[26,27] The synthesis and purification of best performing ruthenium-based dyes for the solar light harvesting devices is expensive. For example, the terpyridine black dye sells at around $3500 per gram.[28] The second problem is the photo-toxicity of the ruthenium-based dyes inviting a potential environmental hazard.[29,30] A detailed study on the mechanism of photo-toxicity of the dyes $Ru(phen)_3^{2+}$ shows that upon illumination extracellular and membrane-bound Ru (II) complex generates singlet oxygen. A local high concentration of singlet oxygen causes a sequence of undesirable events that eventually lead to plasma membrane damage, which is manifested by a loss of membrane integrity and entry of the dye into living cells.[31] In the contest of cost and biocompatibility, porphyrin based solar devices are gaining great interest in the contemporary literature.[32-36] Due to strong absorption of porphyrins in the region of 400-450 nm (Soret band or B) as well as 500-700 nm (Q bands), they find applications in many fields such as photodynamic therapy for the treatment of cancer[37] and photovoltaic conversion of solar energy.[34,35,38-42] Porphyrins and metalloporphyrins have been used for the visible light sensitization of TiO_2 and applied for the degradation of 4-nitrophenol, acetaldehyde, rhodamine B, acid chrome blue K and atrazine.[36,43-47] Though the photocatalysis using porphyrin and metalloporphyrin functionalized TiO_2/ZnO is well documented in the literature, but the knowledge on the fundamental electron transfer dynamics are sparse. The key time scales for the photoinduced ultrafast electron transfer processes in porphyrin and its derivative have great importance due to their biological relevance and also the time scales are the key factor for efficient solar energy conversion.

Porphyrins are able to bind with almost all metal ions, resulting in four to six coordinated metalloporphyrin complexes.[48] Metalloporphyrins are chemically and biologically very important molecules because of their versatile catalytic capabilities. Iron porphyrins under sunlight induce reversible redox processes of the metal centre, mimicking some significant biochemical sequences in the catalytic cycle of the cytochrome P-450 oxygenases.[49-51] The metalloporphyrin excited states that show photochemistry are those involved in charge transfer transitions, either from the axial ligand to the metal centre or from the porphyrin itself to the metal. The reaction mechanism of porphyrin metallation in solution consists of the following steps: deformation of the porphyrin ring, outer sphere association of the solvated metal ion and the porphyrin, exchange of a solvent molecule with the first pyrrolenine nitrogen atom, and chelate-ring closure with the expulsion of more solvent molecules followed by deprotonation of nitrogen atoms, which leads to the formation of the metalloporphyrin.[52] The metallation reactions are generally slow processes which can be attributed to the distortion of the porphyrin ring needed to form the first bonds to the metal.[53,54] Previously, Zewail & coworkers[55] have reported the femtosecond dynamics of Co(II) tetraphenylporphyrin (CoTPP) and ZnTPP where intramolecular electron transfer from porphyrin a_{2u} (π) to Co (d_{z2}) occurs as Co (II) (d^7) facilitates the existence of a low-lying charge transfer (CT) state but in case of Zn, there is no low-lying CT state as Zn has no unoccupied d orbitals. Granados-Oliveros et al.[47] have investigated the photodegradation of atrazine

in aqueous solution and under visible light irradiation in the presence of tetra(4-carboxyphenyl)porphyrin (TcPP) with different metal centres (Fe(III), Cu(II), Zn(II) and metal free) adsorbed on TiO_2 surface. Photocatalytic activity was found only after the addition of hydrogen peroxide and complexes like TcPPFe and TcPPCu containing a central metal ion with unfilled d orbitals show higher photocatalytic activity. Wang et al.[56] have reported the efficient degradation of 4-nitrophenol by using 5,10,15,20-tetra-[4-(3-phenoxy)-propoxy]phenyl porphyrin and 5,10,15,20-tetra-[2-(3-phenoxy)-propoxy]-phenyl porphyrin with Cu(II) as central metal ion under visible light irradiation and proposed that the excited electron at porphyrin LUMO transferred to CB of TiO_2 and then it reduces Cu(II) to Cu(I) and Cu(I) can be reoxidized to Cu(II) by dioxygen species or by hydrogen peroxide produced in solution.

Our present review makes an attempt to explore the key photoinduced dynamics in hematoporphyrin (HP) and protoporphyrin IX (PP) sensitized TiO_2/ZnO and their potential application in visible light photocatalysis (VLP) and dye sensitized solar cell (DSSC). The role of central metal ions such as iron and copper in porphyrin functionalized TiO_2/ZnO and their implications in VLP will also be discussed. We have also explained the role of iron oxidation states in the electron transfer processes. From the practical application point of view, use of porphyrin-based photocatalytic devices for the water decontamination is very important, given the fact that water from natural resources contains metal ions (Fe^{3+} and Cu^{2+} especially). We have explained the synthesis and characterization of PP-ZnO nanohybrid for a flow type photocatalytic solar device for a prototype water decontamination plant using visible light. We have explored the role of metal ions, specifically, iron (III) and copper (II) in the test water with a model contaminant methylene blue (MB), the waste hazardous product from textile industry[57] in the photocatalytic device under visible light.

Results and Discussion

Twin Applications of HP-ZnO Nanohybrids in Efficient VLP and DSSC[40]

In order to understand the key photoinduced dynamics in porphyrin sensitized devices for enhanced solar energy conversion, we demonstrate our studies on HP functionalised ZnO nanorods (NRs) and their potential twin applications in VLP and DSSC. As shown in Figure 1a, bare HP exhibits a strong Soret absorption at 396 nm together with weak Q bands at 500 Q_y (1←0), 533 Q_y (0←0), 569 Q_x (1←0), and 622 nm Q_x (0←0).[58] In this respect, the removal of a metal ion from the center of a porphyrin molecule (which is the case in HP) results in the appearance of these four weak bands in the visible region, which have been assigned to the splitting of doubly degenerate states into the vibration components. Relative to HP, HP-ZnO nanohybrid exhibits a 12 nm bathochromic shift and a weaker intensity of Soret band.[59] The observation indicate the complex formation between HP and ZnO NRs. As shown in Figure 1b, HP molecules are highly emissive. Upon 409 nm excitation, the strong emission of HP was found to be suppressed when anchored to ZnO NRs. The dramatic quenching of HP emission by ZnO NRs observed in the composite film is indicative of the fact that radiative decay becomes a minor pathway. The inset of Figure 1b shows the excitation spectra of bare HP and HP-ZnO nanohybrids monitored at the emission peak (625 nm). The excitation spectra of HP also show parallel maxima at 400 (Soret), 500, 532, and 574 nm. In addition, the excitation spectra for HP-ZnO LHNs also reveal ~12 nm bathochromic shift which is in accordance to the observations made from the absorption spectra. Because of the interference of the absorption of ZnO NRs with the excitation wavelength of 409 nm, it is difficult to obtain a quantitative estimate of HP emission quenching which was further established by monitoring the emission decay of HP and HP-ZnO nanohybrids.

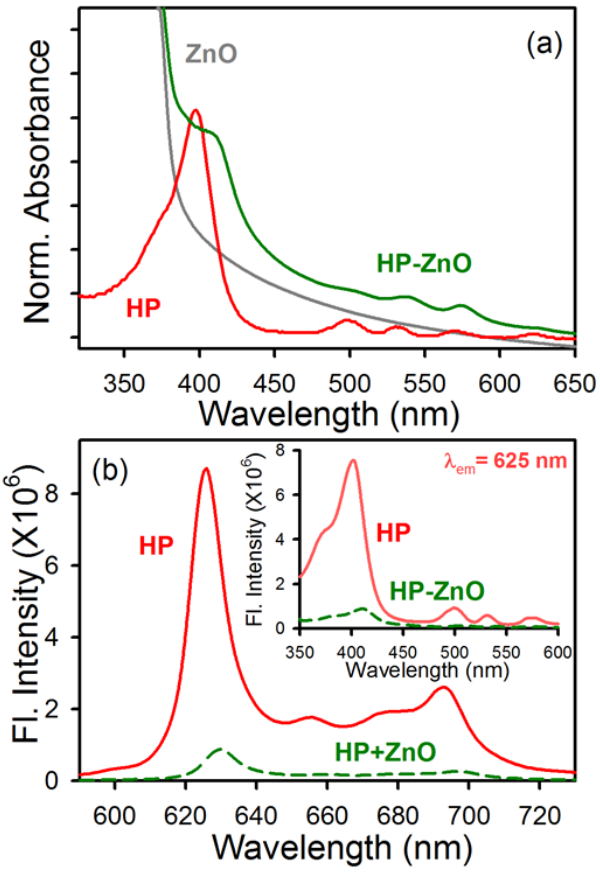

Figure 1. a) UV/Vis absorption spectra of ZnO NRs (gray), HP (red) and HP-ZnO nanohybrids (green) in ethanol. b) Room temperature PL spectra (excitation wavelength was at 409 nm) of bare HP (red) and ZnO-anchored HP (green) are shown. Inset shows the excitation spectra of HP monitored at 625 nm. Reprinted with permission from ACS Appl. Mater. Interfaces 4, 7027-35 (2012). Copyright 2012 American Chemical Society.

As shown in Figure 2, the fluorescence decay curve of HP was fitted with single exponential decay, which showed a lifetime of 10.38±0.06 ns depicting HP molecules were monomeric during the fabrication process.[60] A significant decrease in HP fluorescence lifetime (τ_{avg}) is observed in the presence of ZnO NRs and two fluorescence lifetimes are obtained which are summarized in Table 1. In particular, a faster component of 0.05±0.01 ns generates which contributes nearly 97% of the decay in HP-ZnO composite. Based on the results presented in Figures

1b and 2, we can conclude that an additional nonradiative pathway competes with the fluorescence of excited HP molecules. The apparent rate constant, k_{nr}, is determined for the nonradiative processes by comparing the lifetimes of HP in the absence (τ_0) and the presence (τ) of ZnO NRs, using equation 1.

$$k_{nr} = 1/\langle\tau\rangle - 1/\langle\tau_0\rangle \qquad (1)$$

The apparent rate constant for the nonradiative process is estimated to be $(1.66\pm0.24)\times10^{10}$ s^{-1}. As reported in previous studies, such k_{nr} values represent electron transfer from LUMO of HP to the conduction band of ZnO semiconductor and rules out the possibility of self-quenching due to the aggregation of HP molecules on ZnO surface.[61-63] This indicates that the charge injection between excited HP and ZnO NRs is an ultrafast process and it can be modulated by controlling the nature of anchoring of HP to the semiconductor surface.

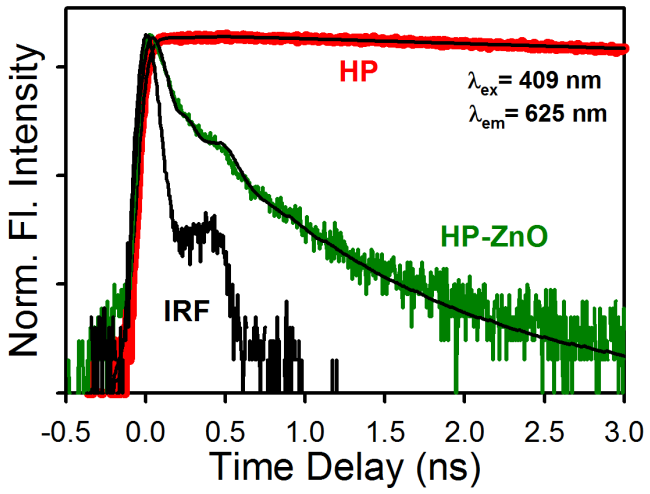

Figure 2. Fluorescence decay profiles of HP-ZnO nanohybrids (green) and free HP (red) in ethanol. Reprinted with permission from ACS Appl. Mater. Interfaces 4, 7027-35 (2012). Copyright 2012 American Chemical Society.

Table 1: Dynamics of picosecond-resolved luminescence transients of HP and HP-ZnO nanohybrids[a]

Sample	τ_1 (ns)	τ_2 (ns)	τ_{avg} (ns)	$k_{nr}\times10^{10}$ (sec^{-1})
HP (bare)	-	10.38±0.06 (100%)	10.38±0.06	-
HP-ZnO	0.05±0.01 (97%)	0.47±0.02 (3%)	0.06±0.01	1.66±0.24

[a]The emission (monitored at 625 nm) was detected with 409 nm laser excitation. k_{nr} represents nonradiative rate constant. Numbers in the parenthesis indicate relative weightages.

The dye used in this study, HP, contains a carboxylic group, which possesses strong binding ability to the surface of ZnO. For the pure dye, the stretching vibration band of carboxylic group are located at 1714 cm^{-1} and 1450 cm^{-1} for antisymmetric and symmetric stretching, respectively, as shown in Figure 3a. After coordinating to ZnO surface, the stretching vibration band of carboxylic group are located at 1693 and 1416 cm^{-1} for antisymmetric and symmetric stretching, respectively. The difference between carboxylate stretching frequencies, $\Delta = \upsilon_{as} - \upsilon_{sym}$ is useful in identifying the bonding mode of carboxylate ligand.[64] Therefore, the Δ value estimated for HP adsorbed on the pure ZnO is found to be (1693-1416) = 277 cm^{-1} which is a much larger value than that of free HP (264 cm^{-1}) and suggests that the binding mode of HP on ZnO is dominantly the monodentate esterlike linkage.

The Raman spectra collected from HP, ZnO NRs and HP-ZnO nanohybrids in the wavenumber region of 300-600 cm^{-1} are shown in Figure 3b. As evidenced from the figure, HP molecules do not show an obvious peak in the experimental range. The Raman spectrum of the ZnO NR arrays exhibits four vibration peaks at 332, 376, 438, and 578 cm^{-1} thus indicating the presence of wurtzite structure.[60,65] The peaks at 376 and 578 cm^{-1} correspond to the polar transverse A_1 and longitudinal E_1 optical phonon mode, respectively; the peak at 332 cm^{-1} is attributed to the E_2^{high}-E_2^{low} mode; and the strong peak at 438 cm^{-1} can be assigned to the nonpolar optical phonon E_2 mode of the ZnO NRs at high frequency, which is associated with oxygen deficiency.[60,66] After binding HP to ZnO, the E_2 mode characteristic band of ZnO, associated to defect centers, is significantly perturbed. This is an indicative of the passivation of ZnO surface states upon HP assembly. The presence of other characteristic bands indicates good retention of ZnO wurtzite structure and crystal shape during the sensitization of ZnO NRs with HP.

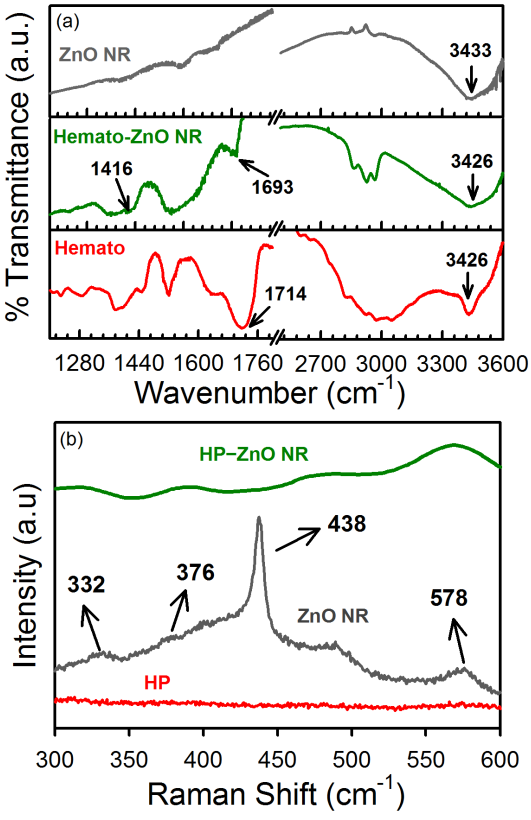

Figure 3. a) FTIR and b) Raman spectra of HP (red), ZnO NRs (gray) and HP-ZnO nanohybrids (green). Reprinted with permission from ACS Appl. Mater. Interfaces 4, 7027-35 (2012). Copyright 2012 American Chemical Society.

In order to apply our findings into a model application, we designed a flow-device consisting of two glass plates (separated by a spacer) as illustrated in materilas and methods for VLP process. The optical response of the visible-light source was found to be effective in the region of 420-950 nm with a maximum intensity at 620 nm. (Figure 4b, inset). The present work identifies a highly stable photocatalytic material, HP-ZnO, which promotes the visible-light sensitized (λ > 420 nm) decomposition of aqueous MB, a representative organic pollutant. Figure 4a shows the change of absorption spectra of MB solution when exposed to visible-light in the absence and the presence of ZnO NRs and HP-ZnO LHNs at two extreme sensitization times, indicating the decolorization of MB during photo-assisted reaction. The histogram (inset) clearly shows that degradation efficiency markedly enhanced in the presence of HP-ZnO nanohybrids, and it also depends on the HP sensitization time and reaches to ~85% upon 24 h of HP sensitization.

In order to confirm that the HP-ZnO induced VLP process occurs via the formation of reactive oxygen species (ROS), the MB photodegradation was performed in Argon (Ar) atmosphere. Under deaerated conditions, a suppression of O_2^{-}• radical

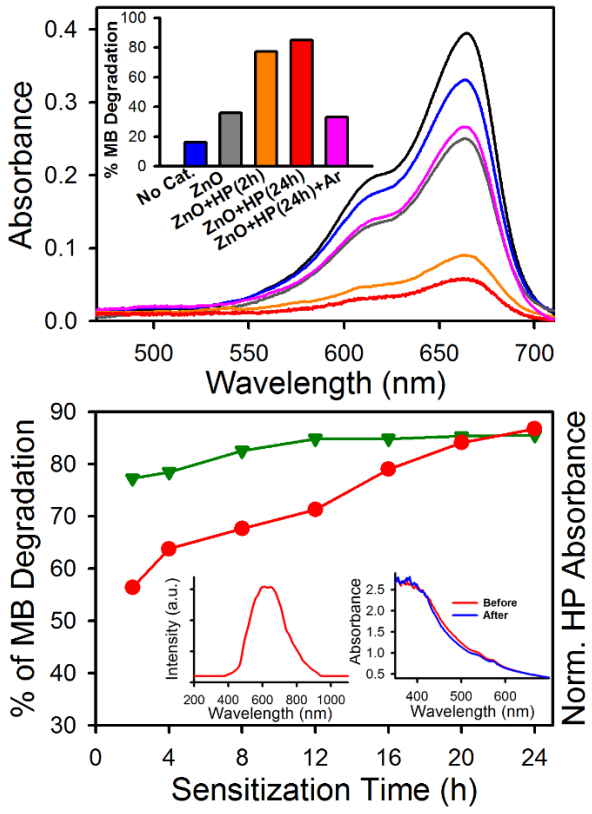

Figure 4. (a) UV-vis spectral changes of aqueous solution of MB in absence and the presence of ZnO, HP-ZnO nanohybrids, under visible-light irradiation. (b) Dependence of photocatalytic activity on the dye-sensitization time. Inset (left) shows the optical response of our visible light source and inset (right) shows the absorbance of HP-sensitized (24 h) ZnO nanohybrids (on a quartz plate) before and after the photocatalysis process. Reprinted with permission from ACS Appl. Mater. Interfaces 4, 7027-35 (2012). Copyright 2012 American Chemical Society.

production occurs and the reducing action of CB electrons is decreased owing to the inhibition of the degradation efficiency of HP-ZnO nanohybrids (24 h) from 85% to 33%. For further understanding the effect of dye-sensitization time on VLP activity, a number of HP-ZnO substrates were prepared with different sensitization periods of 2, 4, 8, 12, 16, 20 and 24 h. Figure 4b shows that the absorption of HP-ZnO LHNs is quite expectedly increased with increasing sensitization times and the catalytic activity also increased due to the higher adsorption of sensitizing dye on ZnO surface which was found to be saturated after 12 h of sensitization time and remain constant thereafter. It is worth noting that the increment of HP concentration must lower the possibility of MB to attach to ZnO surface which would lead to a deterioration of degradation efficiency for increasing HP sensitization time. However, the reverse output again reveals that the bleaching process is followed by ROS formation that are generated at the ZnO surface and subsequently transported to the MB layer. In addition, the photostability of HP-ZnO nanohybrids was verified by measuring the absorbance of HP-ZnO film (on a quartz plate) prior to and after the completion of photocatalysis reaction. As shown in the inset of Figure 4b, after passing 2 mL aqueous solution of MB through the flow-device and 30 min of continuous light irradiation, it was found that a negligible amount of HP leached out from the quartz plate.

The photocurrent density-voltage (J-V) curves of the devices measured under AM 1.5 irradiation (100 mW cm^{-2}) are shown in Figure 5a, and the detailed photovoltaic parameters are summarized in Table 2. The fill factor (FF) and power conversion efficiency (η) of the solar cells are determined from equation (2) and (3),

$$FF = V_M J_M / V_{OC} J_{SC} \qquad (2)$$

$$\eta = V_{OC} J_{SC} FF / P_{in} \qquad (3)$$

where V_M and J_M are the voltage and current density at the maximum power output, respectively, and P_{in} is the intensity of the incident light (100 mW cm^{-2}). The short-circuit photocurrent density (J_{SC}), open-circuit photovoltage (V_{OC}), and FF of a HP-sensitized cell with the iodine-based electrolyte are ~974±48 μA cm^{-2}, 0.42±0.02 V, and 45±0.6 %, respectively, with an overall conversion efficiency, η of 0.20±0.02 %. Note that a well-recognized Ruthenium-based solar cell dye N719 provides η of 0.13±0.01 under the same experimental conditions which is comparable with HP-ZnO based DSSCs.[67]

The incident photon-to-current conversion efficiency (IPCE) for HP-sensitized DSSCs is shown in Figure 5b. The IPCE, defined as the number of electrons collected per incident photon, was evaluated from short-circuit photocurrent (J_{sc}) measurements at different wavelengths (λ), and the IPCE was calculated using equation 4,

$$IPCE\% = \left[1240 \times J_{SC}\left(A/cm^2\right)\right] / \left[\lambda(nm) \times P\left(W/cm^2\right)\right] \times 100 \qquad (4)$$

where P is the incident light power. The IPCE spectra are found to closely resembled the characteristic absorbance spectra of HP

(Figure 1a) which exhibit peaks near 530 and 580 nm due to the Q bands and reaches a maximum value of ~30% at the Soret region (~400 nm), signifying that the HP sensitizers on the photoanode surface are indeed responsible for photocurrent generation.

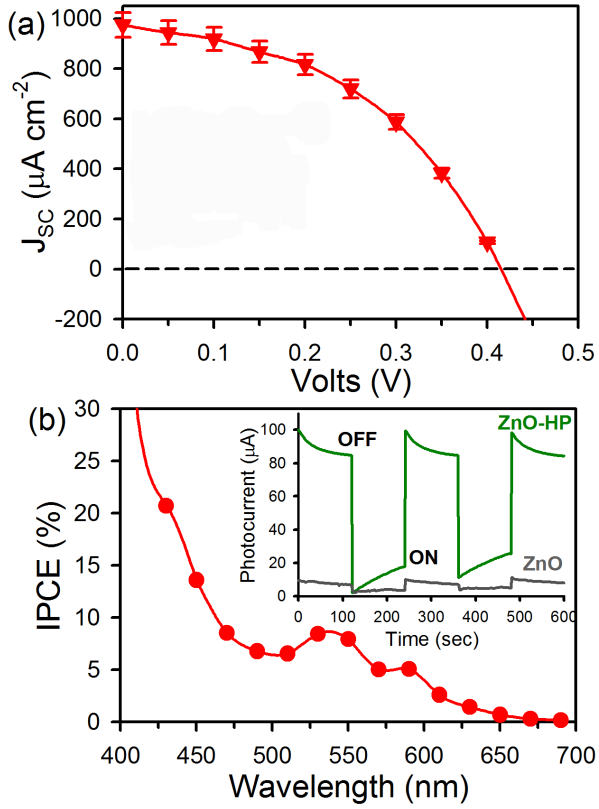

Figure 5. a) Photocurrent-voltage (J-V) characteristics and b) incident photon-to-current conversion efficiency (IPCE) spectra for HP-sensitized ZnO NR-based DSSCs. Inset shows photocurrent responses of ZnO NRs (gray) and HP-ZnO nanohybrid (green) modified FTO electrode under the bias voltage of 2.5 V. The photocurrent was measured across the thickness of the films with 25 mW cm^{-2} incident power from a halogen light source. Reprinted with permission from ACS Appl. Mater. Interfaces 4, 7027-35 (2012). Copyright 2012 American Chemical Society.

Table 2. Device performance[a] of the HP-sensitized DSSCs.

Device	V_{OC} (V)	J_{SC} (μA/cm^2)	FF (%)	η (%)
HP-ZnO	0.42±0.02	974±48	45±0.6	0.20±0.02
N719-ZnO (control)	0.69±0.05	620±33	30±0.5	0.13±0.01

[a]short circuit photocurrent densities (J_{SC}/cm^2), open-circuit voltage (V_{OC}), fill factor (FF), and efficiency (η).

The photoconductivity measurements of bare ZnO and HP-modified ZnO thin films are also performed in order to better understand the photocurrent response of the nanohybrids. At a fixed bias voltage of 5 V, the photocurrent across the thickness of the films were measured by using FTO as one of the electrodes and a small (4 mm diameter) drop of mercury (Hg) on top of the film as a counter electrode. The light source (intensity 25 mW cm^{-2}) was turned ON and OFF every 20 sec, and the obtained current values were continuously recorded using a programmable multimeter (Gwinstek GDM-396). Inset of Figure 5b shows the photocurrent response for the ZnO NR and HP-ZnO thin films, where an improved photocurrent was observed for the HP-modified ZnO thin film (~100 μA) under illuminated condition compared to the bare ZnO NR thin film (~10 μA).

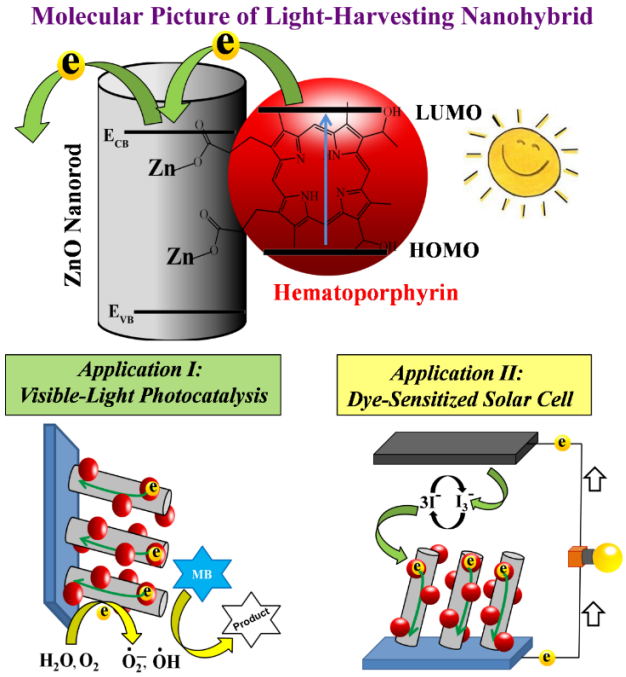

Scheme 1. Schematic representation of a model light-harvesting nanohybrid (LHN) depicting covalently functionalized ZnO NRs with sensitizing dye, Hematoporphyrin (HP). The scheme illustrates the typical absorption process for visible-light in the nanohybrids: light is absorbed by the sensitizing dye HP, transferring an electron into the conduction band of ZnO. The trapped electron in ZnO is exploiting dual vital applications of using HP-ZnO nanohybrid as a model light-harvesting material: (I) visible-light photocatalysis and (II) dye-sensitized solar cell. Reprinted with permission from ACS Appl. Mater. Interfaces 4, 7027-35 (2012). Copyright 2012 American Chemical Society.

Role of Iron Ions and Its Oxidation States in HP Functionalised Titania in Solar Energy Conversion Dynamics[68]

In this section we will explore the photoinduced electron transfer dynamics of HP-TiO_2 nanohybrids in the presence of iron ions in the porphyrin moiety. A typical high-resolution transmission electron microscopic (HR-TEM) image of TiO_2 NPs showing the polycrystalline nature of the particles as in Figure 6a. Lattice fringe of a TiO_2 NP is illustrated which shows an interplanar distance of ~ 0.365 nm, corresponding to the spacing between two (101) planes of anatase TiO_2.[69] The particle sizes are estimated by fitting our experimental TEM data over 55 particles which provides the mean diameter of ~ 6 nm (Figure 6a, inset). In order to determine the complex formation between anchoring group of HP with semiconductor NPs, we have studied UV-vis

spectroscopy as shown in Figure 6b which shows visible light absorption between 400 to 700 nm in HP solution. A strong peak is observed at 397 nm for Soret band together with Q bands between 500-700 nm. HP-TiO_2 nanohybrid exhibits a 3 nm bathochromic shift of Soret band compared to absorption in HP. The bathochromic shift of the soret band is related with different physical and chemical changes in the porphyrin molecular structure when it is incorporated into solids or under specific conditions, in solution. Thus the change in the absorption spectra indicates the formation of HP-TiO_2 complex.

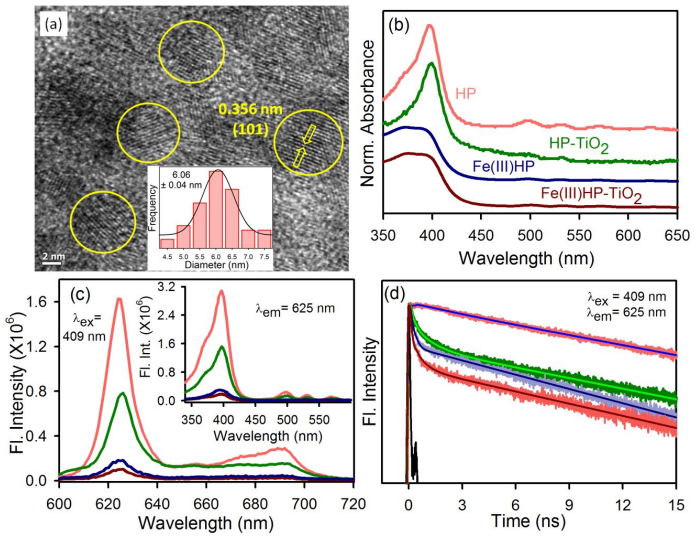

Figure 6. (a) HRTEM image of TiO_2 NPs**.** Inset shows the size distribution of the TiO_2 NPs. (b) UV-Vis absorption of HP (red), HP-TiO_2 nanohybrids (dark green), Fe(III)HP (dark blue) and Fe(III)HP-TiO_2 nanohybrids (dark red) in ethanol. (c) Room temperature PL spectra (excitation wavelength was at 409 nm) of bare HP (red), HP-TiO_2 nanohybrids (dark green), Fe(III)HP (dark blue) and Fe(III)HP-TiO_2 nanohybrids (dark red) are shown. Inset shows the excitation spectra monitored at 625 nm. (d) Fluorescence decay profiles of HP (red), HP-TiO_2 nanohybrids (dark green), Fe(III)HP (dark blue) and Fe(III)HP-TiO_2 nanohybrids (dark red) in ethanol. Phys. Chem. Chem. Phys. 2013, 15, 18562-70. Reproduced by permission of the PCCP Owner Societies.

As shown in Figure 6c, HP presents intense fluorescence emission from two pi orbitals, which encompass the basic tetrapyrrole structure upon excitation with 409 nm laser line. For HP-TiO_2 nanohybrid, there is a considerable decrease in the intensity of the emission peaks in the range of 600-710 nm as compared to bare HP. The decrease in emission intensities can be attributed to quenching by TiO_2 NPs, suggesting an efficient non-radiative photoinduced process from HP to the nanoparticles. The inset of Figure 6c shows the quenching in the excitation spectra of HP upon binding to TiO_2 when monitored at the emission peak (625 nm). The decrease in emission and excitation intensities of HP is also seen in case of Fe(III)HP and Fe(III)HP-TiO_2 nanohybrid. In Fe(III)HP, intramolecular electron transfer occurs from excited HP to Fe(III) leading to the reduction of Fe(III) to Fe(II).[3]

The fluorescence decay of free HP, Fe(III)HP, HP-TiO_2 and Fe(III)HP-TiO_2 in ethanol were obtained upon excitation of 409 nm laser and monitored at 625 nm (Figure 6d). The decay curve of free HP is fitted with single exponential decay with a lifetime of 11.39 ns (Table 3). In case of HP-TiO_2 nanohybrids, the decay curve of HP deviated from single exponential to bi-exponential showing a shorter lifetime 0.40 ns (71%) and longer lifetime 10.68 ns (29%) components. The observed decrease in lifetime could be correlated to the electron transfer process from HP molecules to TiO_2 NPs. The apparent non-radiative rate constant (k_{nr}) is determined by comparing the lifetimes of HP in the absence (τ_0) and in the presence (τ) of TiO_2, using the equation 1.The rate of electron transfer process from excited state of HP to the conduction band of semiconductors is estimated to be 2.08×10^8 s^{-1}. In case of Fe(III)HP, the decay curve of HP is composed of two components, one shorter 0.14 ns (78%) and one longer 8.43 ns (22%) lifetime components. The shorter life time could be correlated to the electron transfer process from HP to Fe(III) ions. In comparison, the decay curve for Fe(III)HP-TiO_2 has three components, two shorter and one longer component. The

Table 3: Dynamics of picosecond-resolved luminescence transients of HP, Fe(III)HP, HP-TiO_2 and Fe(III)HP-TiO_2 nanohybrids[a]

Sample	τ_1 (ns)	τ_2 (ns)	τ_3 (ns)	τ_{avg} (ns)	$k_{nr}\times10^8$ (sec^{-1})
HP (bare)	11.39±0.01 (100%)			11.39 ±0.01	
HP-TiO_2	0.40±0.003 (71%)	10.68±0.02 (29%)		3.38± 0.01	2.08±0.010
Fe(III) HP	0.14±0.002 (78%)	8.43±0.02 (22%)		1.96± 0.003	4.22±0.007
Fe(III) HP-TiO_2	0.09±0.002 (76.4%)	0.40±0.02 (12.5%)	9.74±0.03 (11.1%)	1.19± 0.01	7.52±0.060

[a]The emission (monitored at 625nm) was detected with 409 nm laser excitation. k_{nr} represents nonradiative rate constant. Numbers in the parenthesis indicate relative weightages.

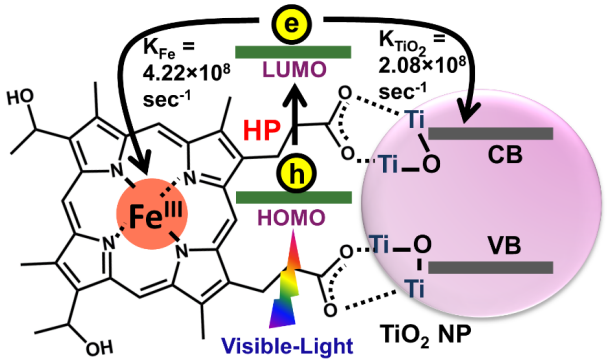

Scheme 2. Schematic representation of ultrafast dynamical processes in hematoporphyrin-titanium dioxide nanohybrid in the presence of iron (III) ions under visible light excitation. Phys. Chem. Chem. Phys. 2013, 15, 18562-70. Reproduced by permission of the PCCP Owner Societies.

shortest component 0.09 ns (76.4%), which is comparable to the shorter component of the decay of Fe(III)HP, shows preferable electron migration pathway from HP to Fe(III) and the second shorter component, 0.40 ns (12.5%), which is similar as in the case of HP-TiO_2, could be correlated to the electron transfer process from HP to TiO_2 NPs. It is clear from the lifetime components that the photoinduced excited electrons in HP of Fe(III)HP-TiO_2 preferably transfer to the Fe(III) ions via nonradiative pathway and the electron transfer rate is estimated to be 7.52×10^8 s^{-1} as shown in scheme 2.

Fourier transform infra-red (FTIR) technique is used to investigate the binding mode of carboxylate group of HP on TiO_2 surface. For free HP, stretching frequencies of carboxylic group are at 1720 cm^{-1} and 1449 cm^{-1} for antisymmetric and symmetric,

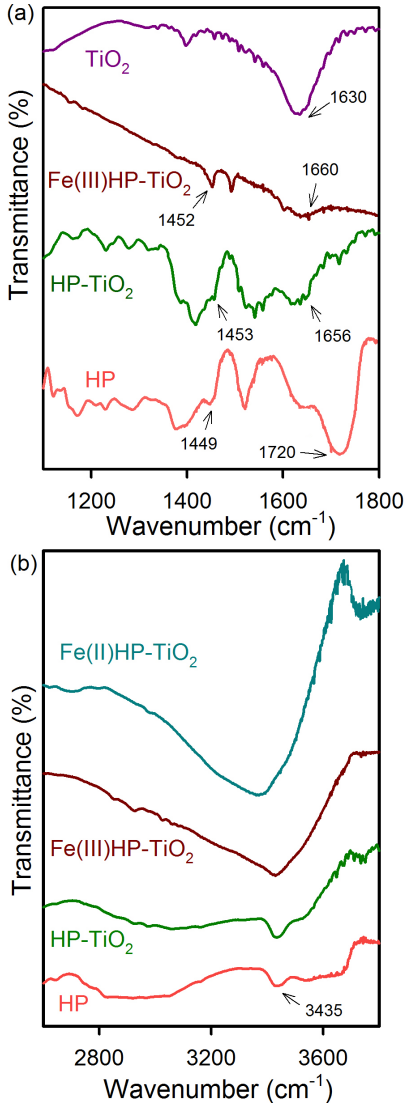

Figure 7. (a) FTIR spectra of HP (red), TiO_2 NPs (dark pink), HP-TiO_2 (dark green) and Fe(III)HP-TiO_2 (dark red). The spectra of HP-TiO_2 and Fe(III)HP-TiO_2 nanohybrids are taken on TiO_2 background. (b) FTIR spectra of HP (red), HP-TiO_2 (dark green), Fe(III)HP-TiO_2 (dark red) and Fe(II)HP-TiO_2 (dark cyan). Phys. Chem. Chem. Phys. 2013, 15, 18562-70. Reproduced by permission of the PCCP Owner Societies.

respectively, as shown in Figure 7a. When HP is attached with TiO_2, the stretching frequencies of carboxylic group are located at 1656 and 1453 cm^{-1} for antisymmetric and symmetric stretching vibration, respectively. The difference between carboxylate stretching frequencies, $\Delta = \upsilon_{as} - \upsilon_{sym}$ is useful in identifying the bonding mode of carboxylate ligand.[64] The observed Δ value for the hybrid material is 203 cm^{-1} which is smaller than that for free HP (271 cm^{-1}). This suggests that the binding mode of HP on TiO_2 is predominantly bidentate. FTIR spectrum of Fe(III)HP-TiO_2 shows that in the presence of iron, HP binds to the TiO_2 NP through bidentate covalent bond. FTIR was also used to investigate the attachment of iron ion to HP molecule. For free HP, the stretching frequency of N-H bond is at 3435 cm^{-1}, as shown in figure 7b. In case of HP-TiO_2 nanohybrid, the N-H stretching frequency of HP remains unperturbed as HP anchors onto TiO_2 surface through carboxylic group. In the presence of iron, the N-H bond is perturbed and became broad which indicates that the Fe ion binds to the HP through the pyrrole nitrogen atoms of the porphyrin. After reduction of Fe(III) to Fe(II), FTIR spectra shows that the N-H bond remain broad which indicates that Fe is still inside the porphyrin ring. The iron oxidation states are evaluated by cyclic voltammetry experiments, as shown in Figure 8. In the presence of Fe(III), a potential for Fe(III)/Fe(II) redox couple is observed at 0.99V vs. Ag/AgCl reference electrode. After treating the Fe(III)HP by sodium borohydride, a reduction potential at - 0.35V was observed which can be attributed to the Fe(II)/Fe(0) redox couple. It is clear that the Fe(III) is reduced to Fe(II) after treating with sodium borohydride.

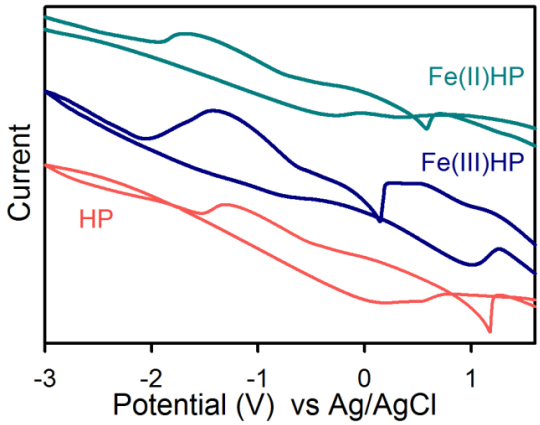

Figure 8. Cyclic voltammograms of HP (red), Fe(III)HP (dark blue) and Fe(II)HP (dark cyan). The CVs were measured in aqueous solution at 0.1 V/s scan rate and Ag/AgCl as reference electrode. Phys. Chem. Chem. Phys. 2013, 15, 18562-70. Reproduced by permission of the PCCP Owner Societies.

According to factor group analysis, anatase TiO_2 has six Raman active modes ($A_{1g} + 2B_{1g} + 3E_g$).[70] As shown in Figure 9a, the Raman spectrum of anatase TiO_2 exhibits six peaks at 150 cm^{-1} (E_g), 198 cm^{-1} (E_g), 396 cm^{-1} (B_{1g}), 515 cm^{-1} (A_{1g}), 520 cm^{-1} (B_{1g}), 640 cm^{-1} (E_g). The Raman spectrum of HP does not show any peak in the wavenumber range of 100-700 cm^{-1}. After binding of HP on TiO_2 surface, the characteristic bands of TiO_2 are all present but slightly blue shifted and broadened which is indicative

of its good retention of the crystal structure and shape. In order to see the differences between the spectra more clearly, the wavenumbers and the full width at half maximum (FWHM) of the bands are given in Table 4. Figure 9a inset shows that the Raman band of TiO_2 at 150 cm^{-1} is shifted to 153 cm^{-1} after binding with HP. The blue shift and broadening of Raman bands of TiO_2 upon binding with HP can be attributed to the attachment of carboxylic group to Ti(IV) that are located at TiO_2 surface.

The X-ray photoelectron spectra of the Ti (2p) regions for bare TiO_2 and HP sensitized TiO_2 are shown in Figure 9b. The Ti ($2p_{3/2}$) binding energy values of TiO_2 and HP-TiO_2 are 458.54 and 458.29 eV respectively. The Ti ($2p_{3/2}$) peak for HP-TiO_2 is shifted to lower binding energy which suggests that Ti atom as the acceptor coordinates with oxygen atom in HP and that the oxygen

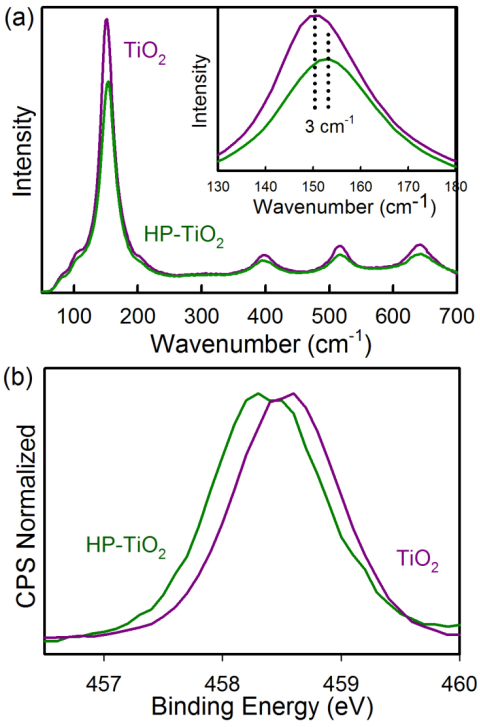

Figure 9. (a) Raman spectra of TiO_2 NPs (dark pink) and HP-TiO_2 nanohybrids (dark green). Inset shows the peaks at 150 cm^{-1}. (b) XPS of the Ti (2p) regions of TiO_2 (dark pink) and HP-TiO_2 (dark green). Phys. Chem. Chem. Phys. 2013, 15, 18562-70. Reproduced by permission of the PCCP Owner Societies.

Table 4. Raman bands and FWHM of TiO_2 and HP-TiO_2

Sample	Raman band (cm^{-1})	FWHM (cm^{-1})
TiO_2	150	21
	396	33
	515	27
	640	38
HP-TiO_2	153	24
	397	36
	517	29
	642	42

atom provides electrons.[45] This suggests that HP molecules are adsorbed on the surface of TiO_2 with carboxyl as the coordinating group.

The photocatalytic degradation of MB in the presence of HP-TiO_2 nanohybrids, Fe(III)HP-TiO_2 nanohybrids and TiO_2 under ultraviolet and visible light was investigated. Under ultraviolet irradiation, 58% MB is degraded in the presence of TiO_2 whereas in the presence of HP-TiO_2 nanohybrids only 30% MB is degraded after 1 h irradiation of light, as shown in Figure 10a. Under UV irradiation, the TiO_2 valence band (VB) electrons are excited to the conduction band which can reduce dioxygen to superoxide, eventually leading to the production of hydroxyl radicals ($OH^{\bullet}$). The HP molecules that are attached to TiO_2 surface cannot simply withstand this severe oxidative stress and it is also degraded. HP acts as an electron scavenger and decreases the MB degradation rate. In the presence of Fe(III)HP-TiO_2 nanohybrids, 83% MB is degraded after 1 h of UV irradiation. The higher degradation rate can be attributed to the presence of Fe(III)HP which can improve the separation of photoinduced e^{-}-h^{+}

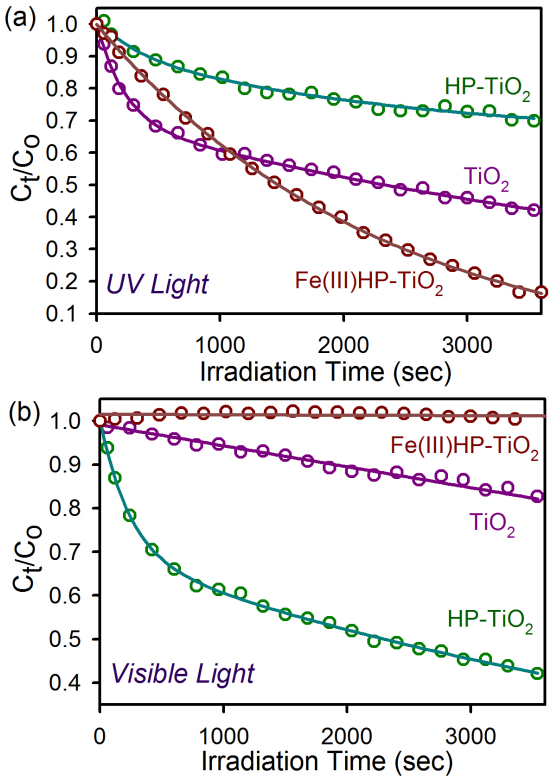

Figure 10. Photocatalytic degradation of MB in the presence of TiO_2 NPs, HP-TiO_2 and Fe(III)HP-TiO_2 nanohybrids under (a) UV light and (b) visible light. Phys. Chem. Chem. Phys. 2013, 15, 18562-70. Reproduced by permission of the PCCP Owner Societies.

pairs.[46] The Fe (III) ion plays an important role in the electron transfer process. Under UV light, TiO_2 VB electrons are excited to the CB and Fe (III) could be reduced to the Fe (II) by capturingthe CB electrons of TiO_2. The reoxidation of Fe (II) to Fe (III) occurs by reducing oxygen to superoxide, eventually leading to the production of hydroxyl radicals ($OH^{\bullet}$). The following set of

reactions explains the enhanced photocatalytic behavior in the presence of Fe (III).

$$Fe(III)HP\text{-}TiO_2 + h\upsilon \rightarrow Fe(III)HP\text{-}TiO_2 (e^-_{cb}, h^+) \quad (5)$$
$$Fe(III)HP\text{-}TiO_2 + e^-_{cb} \rightarrow Fe(II)HP\text{-}TiO_2 \quad (6)$$
$$Fe(II)HP\text{-}TiO_2 + O_2 \rightarrow Fe(III)HP\text{-}TiO_2 + O_2^- \quad (7)$$

Under visible light irradiation, HP-TiO_2 nanohybrid shows highly efficient photocatalytic activity. After 1 h irradiation, it degrades 60% of MB, whereas under same condition bare TiO_2 degraded only 16% of MB. Visible light excites the HP molecules attached to TiO_2 and then the electrons from LUMO of HP inject to the CB of TiO_2. Water in the media acts as an electron donor to regenerate the surface bound sensitizer molecules, which eliminate the need for any undesirable sacrificial electron donors. In the presence of Fe(III)HP-TiO_2, no MB degradation occurred after 1 h under visible light irradiation. In this case, the photoexcited electrons of HP are transferred to the Fe(III) ions instead of TiO_2, which is evident from the TCSPC studies as shown in Figure 6d. The back electron transfer from Fe(II) to HP takes only a few femtoseconds (~ 50fs).[71] Thus (Fe)HP-TiO_2 shows no photocatalytic activity under visible light irradiation.

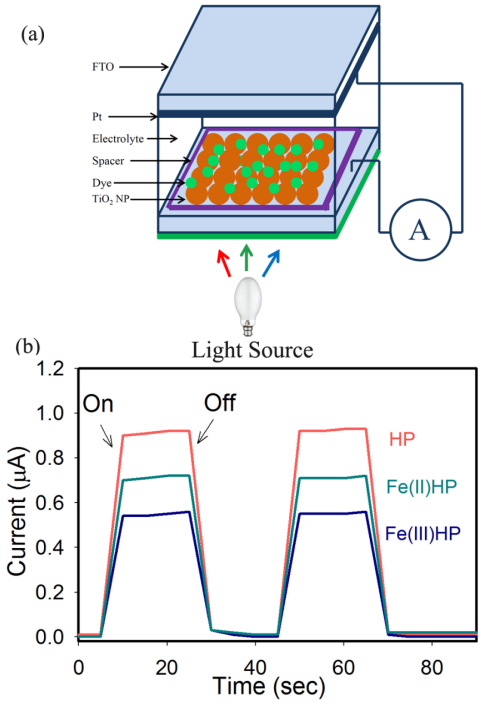

Figure 11. (a) Schematic representation of photocurrent measurement set up using dye-sensitized solar cell geometry. (b) Photocurrent responses of HP (red), Fe(III)HP (dark blue) and Fe(II)HP (dark cyan) sensitized TiO_2 without any bias voltage under 10 mW cm^{-2} incident power irradiation from a light source. Phys. Chem. Chem. Phys. 2013, 15, 18562-70. Reproduced by permission of the PCCP Owner Societies.

The photocurrent measurement of HP-TiO_2 and (Fe)HP-TiO_2 nanohybrids were carried out in order to better understand the electron transfer processes in terms of short circuit current in a solar cell. Photocurrent measurements were done by using DSSC set up as shown in Figure 11a. The light source (10 mW cm^{-2}) was turned on and off every 20 sec and the obtained current values were continuously recorded. Figure 11b shows the photocurrent response of HP, Fe(III)HP and Fe(II)HP sensitized TiO_2, where in the presence of Fe(III), photocurrent was found to decrease when compared to the electrodes sensitized with HP. This agrees well with our observations from the TCSPC and photocatalysis experiments. Photoexcited electrons from HP are transferred to Fe(III) instead of TiO_2 in case of Fe(III)HP sensitized TiO_2 which leads to a decrease in the photocurrent response. When Fe(III) is reduced to Fe(II), the photocurrent increases which indicates that the electrons from excited HP could be favorably transferred to TiO_2 CB.

Role of Dissolved Metal Ions in Test Water in the Porphyrin-Based Applied Materials for Visible Light Photocatalysis[72]

In this section, we will explore the role of metal ions, specifically, iron (III) and copper (II) dissolved in the test water in the extent of their natural abundance in the photocatalytic device under visible light. To make a flow type photocatalytic solar device for a prototype water decontamination plant using visible light, PP-ZnO nanohybrids were synthesized and characterized.

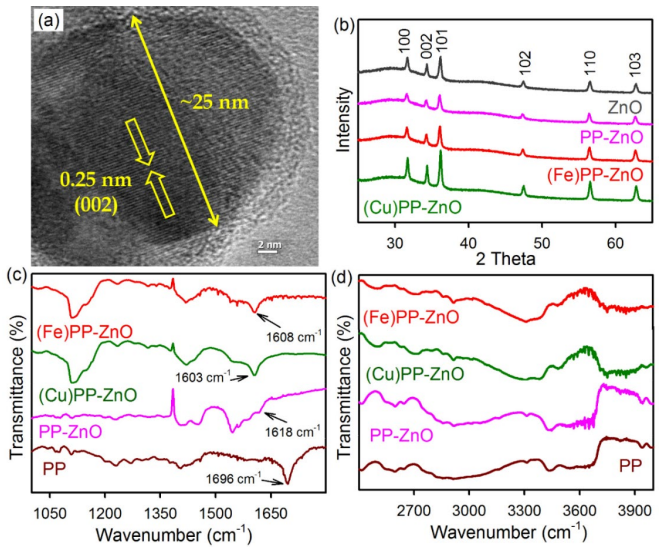

Figure 12. (a) HRTEM images of ZnO NPs. (b) X-Ray diffraction pattern of ZnO(dark gray), PP-ZnO(pink), (Fe)PP-ZnO (red), (Cu)PP-ZnO(green). (c) FTIR spectra of PP (brown), PP-ZnO (pink), (Cu)PP-ZnO (green), (Fe)PP-ZnO (red). The spectra of PP-ZnO, (Fe)PP-ZnO and (Cu)PP-ZnO are taken on ZnO background. (d) FTIR spectra of PP (brown), PP-ZnO (pink), (Cu)PP-ZnO (green) and (Fe)PP-ZnO (red). Chem. Eur. J. DOI: 10.1002/chem.201402632. Copyright 2014 WILEY-VCH Verlag GmbH & Co. KGaA, Weinheim.

A typical high-resolution transmission electron microscopic (HR-TEM) image of ZnO NPs is shown in Figure 12a. From the TEM study an average size of 25 nm ZnO NPs were observed. The TEM study on a single NP also reveals crystal fringes of an inter-planar distance of 0.26 nm corresponding to the spacing between two (002) planes of ZnO.[73] The XRD study (Figure 12b) on the bare ZnO NPs (2θ range from 20° to 70°) and upon sensitization with PP in the absence and presence of the metal ions

(Fe(III), Cu(II)) shows characteristic planes of ZnO (100), (002), (101), (102), (110) and (103). Intactness of the crystal planes of ZnO upon sensitization of the PP dye and metal ions is also clear from the study.

Fourier transform infrared (FTIR) spectroscopy has been used to confirm the binding mode of PP on the ZnO surface. For free PP, stretching frequencies of carboxylic group are located at 1696 cm^{-1} and 1402 cm^{-1} for antisymmetric and symmetric stretching vibration, respectively, as shown in figure 12c. In case of PP-ZnO, the stretching frequencies are located at 1618 cm^{-1} and 1405 cm^{-1} for antisymmetric and symmetric stretching vibration, respectively, providing clear evidence for the de-protonation of the carboxylic group upon addition of ZnO NPs. The difference between carboxylate stretching frequencies, $\Delta=\nu_{as}-\nu_{sym}$ is useful in identifying the binding mode of the carboxylate ligand.[64] The observed Δ value for the PP-ZnO nanohybrid is 213 cm^{-1} that is smaller than that of free PP (294 cm^{-1}). This suggests that binding mode of PP on ZnO is predominantly bidentate. However, Fe (III) and Cu (II) incorporated nanohybrids also show bidentate covalent binding of PP to ZnO NPs through carboxylic groups. The N-H stretching frequency has been used to investigate the attachment of the metal ions to the PP associated with the host ZnO. For free PP, N-H stretching frequency is at 3441 cm^{-1}(Figure 12d). In case of PP-ZnO nanohybrid, the N-H stretching frequency of the PP cavity remains unperturbed as PP anchors onto the ZnO surface through carboxylic group. In the presence of iron and copper, the N-H bond is perturbed which indicate that iron (III) and copper (II) bind to the PP through pyrrole nitrogen atoms of the porphyrin.[68]

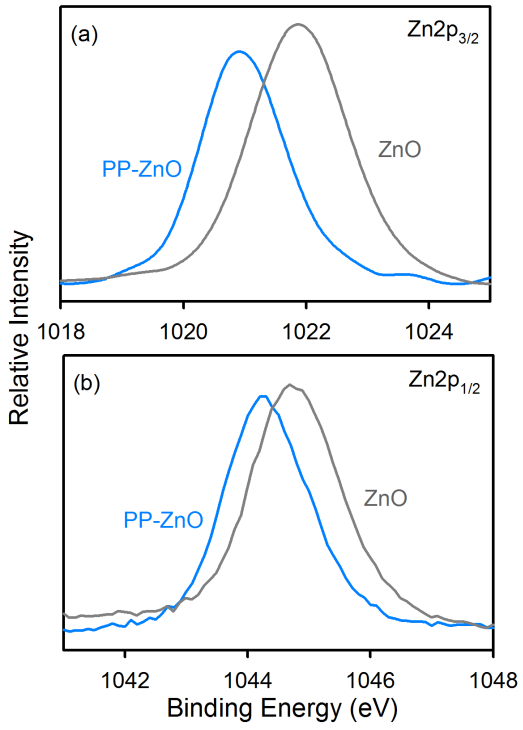

Figure 13.: a) $Zn2p_{3/2}$ and b) $Zn2p_{1/2}$ XPS of ZnO and PP-ZnO Nanohybrids. Chem. Eur. J. DOI: 10.1002/chem.201402632. Copyright 2014 WILEY-VCH Verlag GmbH & Co. KGaA, Weinheim.

The assembly of PP molecules on ZnO NRs and their surface interactions are also confirmed by X-ray photoelectron spectroscopy (XPS), as shown in Figure 13. The typical Zn2p XPS of ZnO NPs show a doublet structure due to the spin-orbit splitting, which was assigned to the $2p_{3/2}$ and $2p_{1/2}$ with a separation of binding energy of 22.91 eV. The $Zn2p_{3/2}$ (Figure 13a) binding energy values of ZnO and PP-ZnO hybrid are 1021.86 and 1020.93 eV, respectively. In addition, the binding energy for $Zn2p_{1/2}$ (Figure 13b) of the PP-ZnO hybrid is shifted from 1044.77 to 1044.25 eV, thereby indicating the existence of chemical bonds between ZnO and PP. These data suggest that Zn atom acts as the acceptor coordinating with oxygen atom in PP-ZnO system where the oxygen atom provides the electrons for bonding.[60] These results are consistent with the observations enumerated from FTIR, and further confirm that the nanohybrids of PP-ZnO are formed through covalent binding between ZnO NPs and PP.

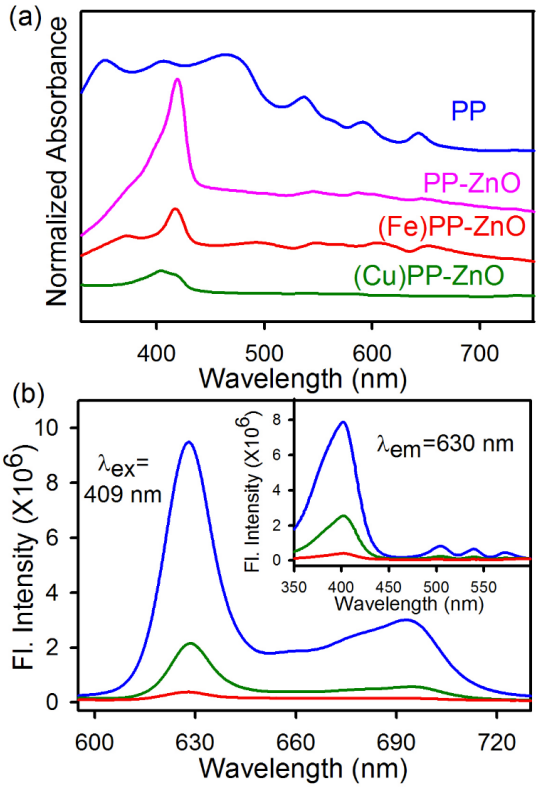

Figure 14. (a) UV-Vis absorption spectra of PP(blue), PP-ZnO(pink), (Fe)PP-ZnO (red), (Cu)PP-ZnO (green) in DMSO-water (V/V). (b) Room temperature PL spectra of PP(blue), PP-Cu(green), PP-Fe(red) are shown in DMSO-water mixture(V/V). Inset shows excitation spectra monitored at 630 nm. Chem. Eur. J. DOI: 10.1002/chem.201402632. Copyright 2014 WILEY-VCH Verlag GmbH & Co. KGaA, Weinheim.

PP having extensively delocalized π electrons shows a soret band ($S_0 \rightarrow S_2$) and Q bands ($S_0 \rightarrow S_1$) due to π-π^* electronic transition. UV-Vis absorption spectra of PP in DMSO-water clearly indicate formation of H- and J- type of aggregate due to presence of peaks at 352 nm and 465 nm, respectively (Figure

14a, blue spectrum).[74,75] The soret band peak of PP resides at 405 nm while Q band peaks are observed in the range between 500nm-650nm. The disappearance of the aggregate peak at 463 nm, red-shift in the soret band (405 to 421 nm, pink spectrum in figure 14a) are indicative of the direct interaction of PP with ZnO nanoparticles.[47,76] As shown in figure 14b, PP in DMSO-waterexhibits a strong emission at 630nm and 700nm upon excitation soret band by a laser source at 409 nm. However, after metalation with Fe (III) and Cu (II), steady state emission of PP is

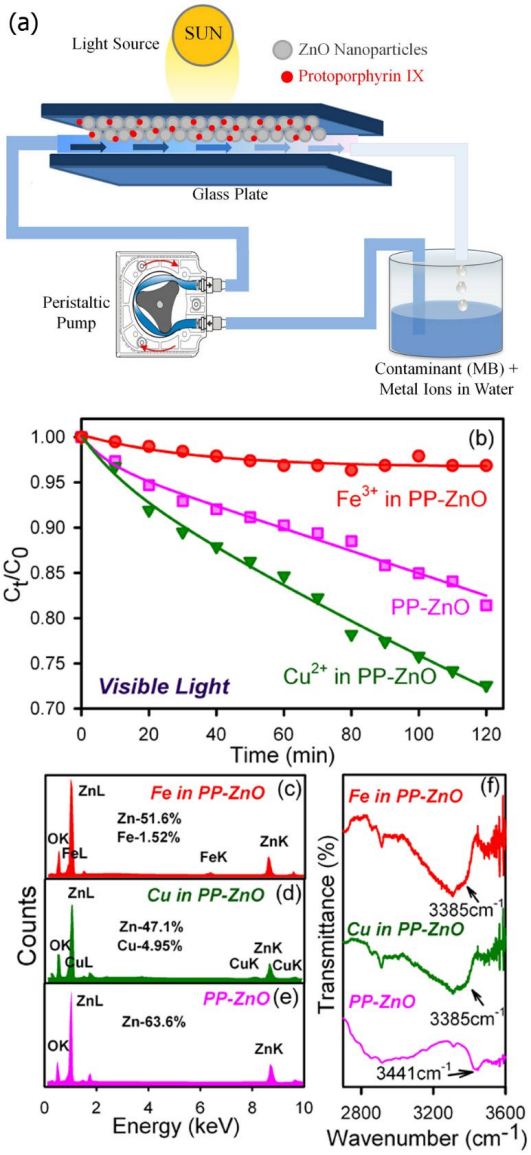

Figure 15. (a) Schematic representation of the developed flow device for photocatalysis. (b) Photocatalytic degradation of MB in the above flow device using PP-ZnO as photocatalyst in the presence of Cu^{2+} (dark green), Fe^{3+} (red) as contaminants in MB solution and without any metal ions (Pink). EDAX spectra of PP-ZnO (pink, e) in the presence of Cu^{2+} (dark green, d) and Fe^{3+} (red, c). (f) FTIR spectra of PP-ZnO (pink) before photocatalysis and after photocatalysis in the presence of Cu^{2+} (dark green) and Fe^{3+} (red). Chem. Eur. J. DOI: 10.1002/chem.201402632. Copyright 2014 WILEY-VCH Verlag GmbH & Co. KGaA, Weinheim.

significantly decreased indicating non-radiative processes which can be attributed to the fast intersystem crossing to the excited triplet state.[77] In addition, charge-transfer processes are also concluded to be responsible for the quenching.[78]

Figure 15a shows a prototype photo-device for the investigation of photocatalytic efficiency of the nanohybrid under visible light irradiation. The details of the device may be found in our earlier publication.[79] The test water under investigation contains methylene blue (MB), model water contaminant in absence and presence of iron and copper metal ions (44.5 mg/L copper and 9.2 mg/L iron). From the data shown in figure 15b, the presence of the iron ion in water significantly decreases the photocatalytic efficiency, whereas the copper on the other hand enhances the degradation of MB within our experimental time window 2 hours. Our observation is consistent with the literatures.[68,80] Oliveros et al.[47] have investigated the photodegradation of atrazine in aqueous solution under visible light irradiation in the presence of tetra(4-carboxyphenyl)porphyrin (TcPP) in absence/presence of different central metal ions (Fe(III), Cu(II), Zn(II)) adsorbed on TiO_2 surface and the maximum photocatalytic activity was obtained using Cu(II) porphyrin as photosensitizer after the addition of hydrogen peroxide. The concentration of metal ions, we have used in the present study (44.5 mg/L copper and 39.2 mg/L iron) is in the order of given by the world health organization (WHO)

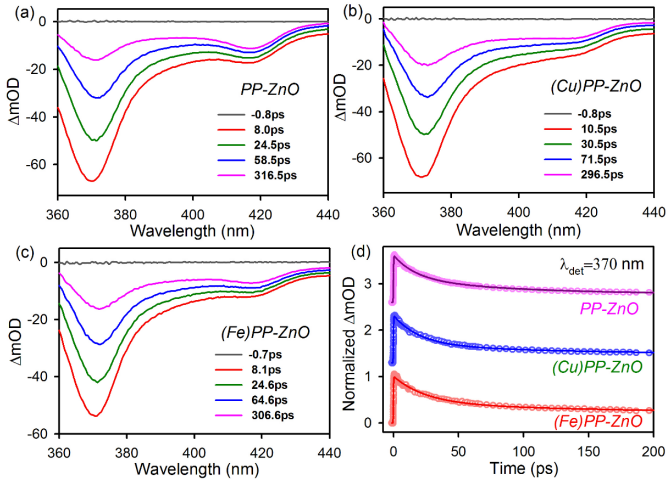

Figure 16. Transient absorption spectra of (a) PP-ZnO (b) (Cu)PP-ZnO and (c) (Fe)PP-ZnO at different time delays after excitation at 350nm. (d) Time-resolved absorption changes of PP-ZnO (pink), (Cu)PP-ZnO (blue), (Fe)PP-ZnO (red) at probe wavelength 370nm. All the spectra are studied in DMSO-water mixture (V/V). Chem. Eur. J. DOI: 10.1002/chem.201402632. Copyright 2014 WILEY-VCH Verlag GmbH & Co. KGaA, Weinheim.

recommended value in the drinking water (30 mg/L copper and 10 mg/L iron) available in the natural resources. The energy-dispersive X-ray spectroscopy (EDAX) of PP-ZnO before and after 2 hours of photocatalysis in the presence of copper and iron ions are shown in figure 15c-e which clearly indicates the presence of metal ions on the catalyst surface after photocatalysis. The complexation rate of copper with PP is higher than that of iron which is responsible for the presence of higher copper (4.95%) on PP-ZnO than iron (1.52%).[81] To confirm the complex

Table 5. Results of the fits of the transient absorption data at different probe wavelengths

Sample	Monitored Wavelength(nm)	τ_1 (ps)	τ_2 (ps)	τ_3 (ns)
PP-ZnO	370	16.91 (48.63%)	88.64 (34.14%)	7.44 (17.27%)
	415	6.00 (24.44%)	45.81 (26.54%)	1.60 (49.02%)
	543	3.73 (40.05%)	60.00 (29.92%)	1.60 (30.03%)
	590	5.84 (31.68%)	60.00 (26.11%)	1.60 (42.21%)
PP-Cu-ZnO	370	16.20 (51.10%)	90.00 (30.98%)	7.85 (17.92%)
	415	5.69 (27.87%)	61.45 (33.27%)	1.60 (38.86%)
	543	3.59 (23.68%)	27.52 (49.70%)	1.60 (26.62%)
	586	5.10 (31.20%)	40.93 (33.64%)	1.60 (35.16%)
PP-Fe-ZnO	370	25.00 (58.29%)	204.23 (22.99%)	11.01 (18.72%)
	415	15.00 (34.16%)	201.73 (17.90%)	1.60 (47.94%)
	550	13.41 (41.38%)	200.00 (7.56%)	1.60 (51.06%)
	590	13.06 (34.31%)	220.00 (11.82%)	1.60 (53.87%)

formation, FTIR studies were done as shown in figure 15f. For PP-ZnO, N-H stretching frequency is at 3441 cm^{-1}. In the presence of iron and copper, the N-H bond is broadened and shifted to 3385 cm^{-1} which indicate that iron (III) and copper (II) bind to the PP through pyrrole nitrogen atoms of the porphyrin. Thus the metal ions present in the contaminant solution are complexing with the PP. After 2 hours of photocatalysis, ~5-10% PP is leaching out from the ZnO surface. The observation clearly necessitates the exploration of ultrafast dynamical studies on the nanohybrid.

The femtosecond-resolved transient absorption spectra (excitation wavelength = 350 nm) of the PP-ZnO nanohybrid in the presence and absence of iron and copper ions are shown in the wavelength range of 360-440 nm in figure 16a-c. It should be noted that the peaks at 370 nm and ~415 nm correspond host ZnO band gap (3.37 eV) and soret band of the guest PP, respectively. The decay profiles at 370 nm detection wavelength revealing ground state recovery of the excited ZnO in the nanohybrid in presence and absence of the metal ions are shown in figure 16d. The interference of PP absorption at the detection wavelength (370 nm) was ruled out in a set of control experiments with pure PP, revealing different time scale (~ns) of ground-state bleach recovery. The numerical fitting of the transient absorption data of PP-ZnO shows decay time constants of 16.91 ps (48.63%), 88.64 ps (34.14%) and 7.44 ns (17.27%) for the ground state recovery of the host ZnO in the nanohybrid. While the nanohybrid in presence of copper ion shows similar recovery time constants (16.20 ps (51.10%), 90.00 ps (30.98%) and 7.85 ns (17.92%)), a significant retardation of the time in presence of the iron ions are observed (25.00 ps (58.29%), 204.23 ps (22.99%) and 11.01 ns (18.72%)). The time constants imply that the presence of iron ions can separate the electron-hole pairs of the excited ZnO NPs efficiently, leading to the slow recovery of the ground state of

ZnO NPs in the nanohybrid. The transient absorption spectra of the Q bands of PP in the nanohybrids in wavelength range 465-660 nm are shown in figure 17a, c, e. From this figure it is evident that the four number of Q bands present in the free base PP became essentially two in the presence of the iron and copper ions due to the higher molecular symmetry (D_{4h}).[82] The decay profiles at soret and Q bands revealing the ground state recovery of the excited PP in the nanohybrid in the presence and absence of metal ions are shown in the figure 17b, d, f. The decay time constants are shown in the table 5. From the table 5 and figure 17, it is clear that the presence of iron (III) ion delays the recovery of the excited PP, whereas, presence of copper ion exhibits similar time constants compared to PP in the nanohybrid. From the above observation on the ground state recovery dynamics, it is expected that upon UV excitation of ZnO in the nanohybrid in presence of iron ion the charge transfer is facilitated (longer exciton lifetime) and expected to reveal better photocatalysis.[46]

The fluorescence decays of PP and PP-ZnO nanohybrid in absence and presence of iron and copper ions are shown in figure 18a and 18b (shorter time window) upon excitation of 409 nm and monitored at 630 nm. The fluorescence transients of PP and (Cu)PP are fitted with single exponential decays with a lifetime of 16.03 ns and 17.29 ns, respectively (table 6). The increase in the

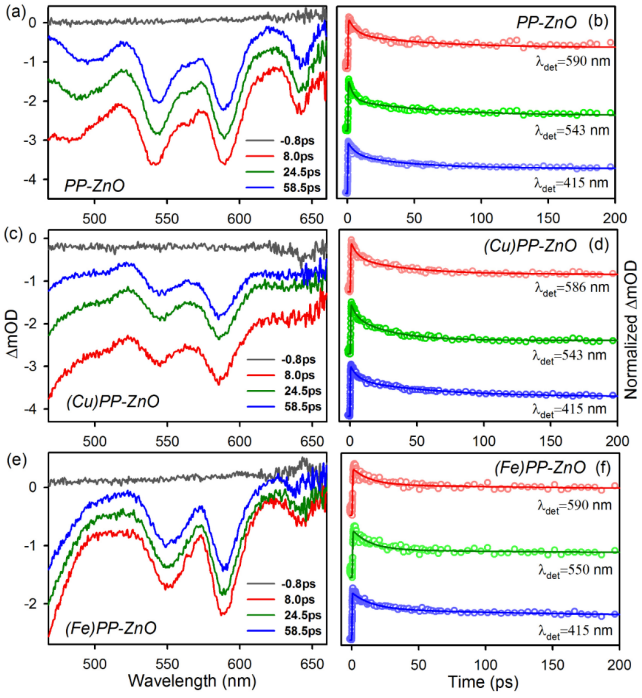

Figure 17. Transient absorption spectra of (a) PP-ZnO, (c) (Cu)PP-ZnO and (e) (Fe)PP-ZnO) at different time delays after excitation at 350nm. Time-resolved absorption changes of (b) PP-ZnO (d) (Cu)PP-ZnO and (f) (Fe)PP-ZnO at different probe wavelength. All the spectra are studied in DMSO-water mixture (V/V). Chem. Eur. J. DOI: 10.1002/chem.201402632. Copyright 2014 WILEY-VCH Verlag GmbH & Co. KGaA, Weinheim.

excited state lifetime of PP in the presence of copper ion may be indicative of the stability of the PP molecule as reported earlier.[80] The time-resolved data of (Cu)PP rules out the possibility of charge transfer transitions from PP to Cu ion and thus the steady state quenching of the PP emission in the presence of Cu can be attributed to the fast intersystem crossing which is beyond our experimental time window.[77] However, the fluorescence decay profile of PP in the presence of iron (III) shows shorter time constants of 0.048 ns (50%) and 2.34 ns (5.95%) along with 16.61 ns (44.05%) with an average excited state lifetime of 7.48 ns.

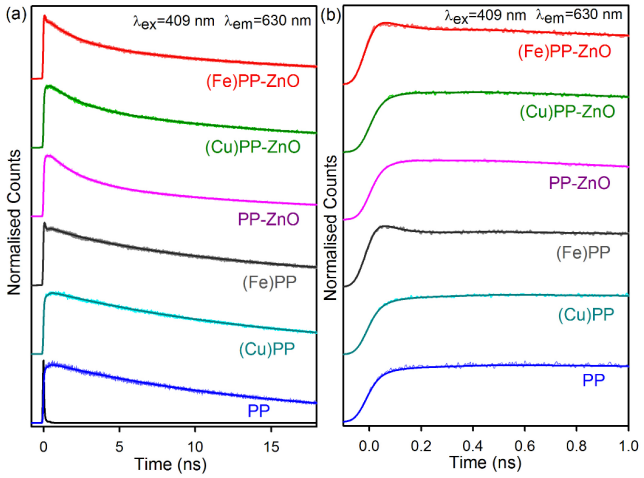

Figure 18. Fluorescence decay profile of PP (blue), Cu-PP (cyan), Fe-PP (dark gray), PP-ZnO (pink), (Cu)PP-ZnO (green), (Fe)PP-ZnO (red) in (a) longer time window and (b) shorter time window. All the spectra are studied in DMSO-water mixture (V/V). Chem. Eur. J. DOI: 10.1002/chem.201402632. Copyright 2014 WILEY-VCH Verlag GmbH & Co. KGaA, Weinheim.

The faster excited state lifetime of the PP in presence of iron ion could be correlated to the electron transfer process from PP to iron ion.[68] The apparent nonradiative rate constant (k_{nr})[83] is determined by comparing the lifetimes of PP in the absence (τ_0) and in the presence (τ) of acceptor, using the equation 1. As shown in figure 18, in PP-ZnO nanohybrid, the fluorescence decay profile is composed of a faster component of 2.06 ns (56.25%) and a longer component of 16.77 ns (43.75%), indicating an electron transfer process from PP molecule to the ZnO NPs. While the slower component is consistent with the excited state lifetime of PP without ZnO, the faster one may be rationalized the electron migration time from PP to the host ZnO.[84] In presence of copper ion the excited state dynamics of the nanohybrid essentially remains unaltered. However, in presence of iron (III), the decay profile of PP-ZnO shows an additional time component of 0.024 ns (54.29%), which is absent in either PP-ZnO and PP-ZnO in presence of copper ion and can be rationalized as electron migration pathway from PP to centrally located Fe(III).

In order to understand the modulation of photocatalysis of PP-ZnO in presence of dissolved metal ions under visible light irradiation as described in figure 15 with our photo-device, we have performed in vitro photocatalysis measurement of the

Table 6. Picosecond-resolved fluorescence transients of PP, (Fe)PP, (Cu)PP, PP-ZnO,(Fe)PP-ZnO and(Cu)PP-ZnO composites.[a]

Sample	τ_1 (ns)	τ_2 (ns)	τ_3 (ns)	τ_{avg} (ns)	$k_{nr}\times10^7$ (S^{-1})
PP	16.03±0.01 (100%)			16.03 ±0.01	
(Fe)PP	16.61±0.05 (44%)	2.34±0.10 (6%)	0.048±0.01 (50%)	7.48± 0.03	7.12± 0.05
(Cu)PP	17.29±0.01 (100%)			17.29 ±0.01	
PP-ZnO	16.77±0.06 (43.7%)	2.06±0.01 (56.3%)		8.50± 0.03	5.52± 0.04
(Fe)PP-ZnO	16.64±0.0 (19%)	2.02±0.01 (26.7%)	0.024±0.01 (54.3%)	3.72± 0.01	20.63 ±0.13
(Cu)PP-ZnO	16.98±0.05 (63%)	2.06±0.01 (37%)		11.47 ±0.04	2.48± 0.03

[a]The emission (monitored at 630 nm) was detected with 409 nm laser excitation. k_{nr} represents nonradiative rate constant. Numbers in the parenthesis indicate relative weightages.

nanohybrid with pre-included metal ions (12 hours incubation time) in quartz cuvette under visible light as displayed in figure 19a. The inclusion of iron ion in the PP-ZnO nanohybrid significantly reduced the photocatalytic efficiency for the degradation of MB under visible light irradiation compared to that in the case of nanohybrid without metal and with copper ion. Relatively efficient photocatalysis of the nanohybrid with copper ion may be correlated with the additional structural stability of the PP in the nanohybrid.[80] After 1 hour visible light irradiation, 55% of MB was degraded in the presence of PP-ZnO. However, the presence of copper ion enhances the photocatalytic activity and 80% MB degradation was observed. The copper ion provides stability to the PP moiety attached to the ZnO NPs, which leads to the enhancement in the photocatalytic activity. The photocatalytic activity of the PP-ZnO nanohybrid was suppressed significantly in the presence of iron ions and only 17% MB degradation was observed. In this case, the photoexcited electrons of PP were trapped in the Fe(III) ions preferably instead of ZnO, which is evident from the transient absorption (figure 17) and TCSPC studies (Figure 18). The observation is consistent with the results obtained using prototype flow device as shown in figure 15. Our transient absorption studies on the nanohybrid at 350 nm excitation reveals longer excitonic lifetime in presence of iron ion compared to that of either without metal or with copper ion. As mentioned earlier, incorporation of iron in the central cavity of the porphyrin under UV light irradiation is expected to offer better photocatalysis in contrast to that of the case under visible light irradiation. Another important fact is that any solar device should be exposed with some amount of UV radiation present in solar light (4-5%). Thus in order to investigate the role of UV excitation, we have performed the photocatalytic activity of the nanohybrid in presence and absence of metal ions under UV light irradiation as shown in figure 19b. Under UV light irradiation, 55% MB degradation observed in the presence of ZnO NPs,

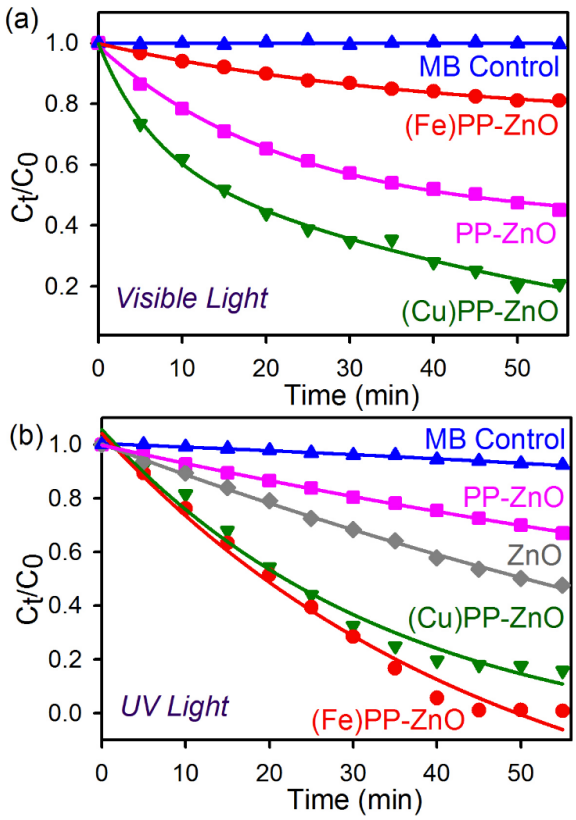

Figure 19. Photocatalytic degradation of MB in presence of ZnO (dark gray), PP-ZnO (pink), (Fe)PP-ZnO (red), (Cu)PP-ZnO (green) and only MB (blue) nanohybrids under the (a) visible light and (b) UV light irradiation. Chem. Eur. J. DOI: 10.1002/chem.201402632. Copyright 2014 WILEY-VCH Verlag GmbH & Co. KGaA, Weinheim.

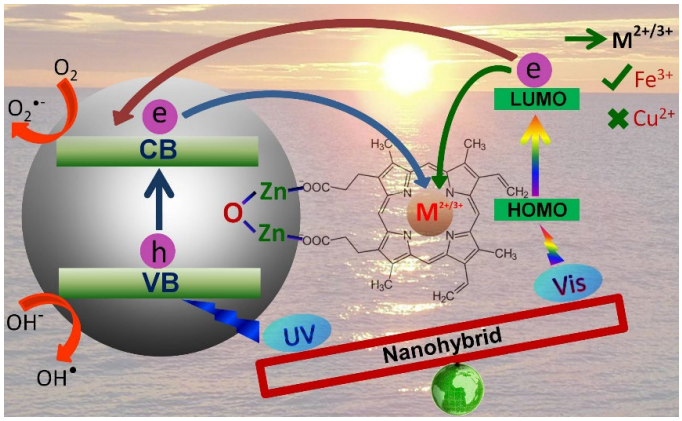

Scheme 3. Schematic representation of ultrafast dynamical processes in protoporphyrin-zinc oxide nanohybrid in the presence of different central metal ions under UV and visible light excitation. Chem. Eur. J. DOI: 10.1002/chem.201402632. Copyright 2014 WILEY-VCH Verlag GmbH & Co. KGaA, Weinheim.

whereas, in the presence of PP-ZnO nanohybrid only 25% MB degradation was evidenced. Thus, the efficiency of the nanohybrid essentially depends on the number of photo-generated carrier (electrons and holes) and their exciton lifetime. In the case of (Fe)PP-ZnO the photo-generated electron is shown to be trapped in the centrally located iron moiety of the nanohybrid and ROS generation is essentially governed by hole in the valence band and enhanced exciton lifetime (as evidenced from transient absorption, discussed above). On the other hand for (Cu)PP-ZnO, ROS generation is expected to be governed by the photo-generated carriers (both electrons and holes), however, it may not acquire extra-advantage from the exciton lifetime (as evidenced from transient absorption), revealing comparable photocatalysis with respect to that in the (Fe)PP-ZnO nanohybrid. The significant retardation of photocatalysis in the case of PP-ZnO without metalation may be rationalized from the photo-reduction of the attached PP by the photo-excited electron from ZnO. We have observed significant photo-bleaching of PP in PP-ZnO nanohybrid in absence of metal ions under UV irradiation. The overall mechanistic pathway of the photo-catalysis of the nanohybrid upon visible and UV irradiation is shown in scheme 3.

Conclusion

The review is an effort to unravel the ultrafast electron transfer dynamics in porphyrin and metalloporphyrin sensitized solar energy harvesting devices. The role of central metal ions, especially iron and copper in the electron transfer processes in the porphyrin sensitized devices is also explored in the review. In one of the studies, Hematoporphyrin (HP) has been conjugated onto covalently functionalized ZnO NRs, forming electron donor-acceptor HP-ZnO nanohybrid which is being established as a potential light harvesting material. The new hybrid nanomaterial has been methodically characterized with the aid of standard optical techniques. Steady-state and picosecond-resolved fluorescence measurements reveal efficient quenching of HP fluorescence in the HP-ZnO nanohybrid suggesting photoinduced charge transfer takes place from LUMO of HP to the conduction band of ZnO. Utilizing this phenomenon, a new dye-sensitized system, incorporating HP on ZnO, is realized for the photodegradation of aqueous organic pollutants under visible light irradiation and a photoelectrochemical cell is constructed, with IPCE values as large as 30%. In another study, picosecond resolved fluorescence studies on HP-TiO_2 nanohybrids in the presence of Fe^{3+} ions suggest that photoinduced electron transfer takes place preferably from LUMO of HP to the Fe(III) instead of CB of TiO_2. Under UV light irradiation, Fe(III)HP-TiO_2 nanohybrid shows higher photocatalytic activity due to the cooperative functions of Fe(III)HP and TiO_2 in generating active species. HP-TiO_2 nanohybrids show higher photocatalytic activity under visible light due to the absence of Fe(III) ions which obstructs the electron transfer from HP to TiO_2. Photocurrent measurements show the role of iron oxidation states in electron transfer processes. From the practical application point of view, water from natural resources contains metal ions (Fe^{3+} and Cu^{2+} especially). To investigate the role of dissolved iron and copper ions in the test water based on their natural abundance (WHO prescribed), we have synthesized and characterized a protoporphyrin IX-ZnO nanohybrid (PP-ZnO) for potential applications in a prototype photo-device for decontamination of test water. Femtosecond time-resolved transient absorption studies

clearly unravel the key time component associated with ground state recovery of the sensitized PP upon metalation for the change of overall photocatalytic efficiency. To our understanding, this detailed spectroscopic study will potentially find its relevance in the large-scale use of the non-toxic and less expensive porphyrin and metallopophyrin-based nanohybrids for the visible-light photocatalysis and photovoltaics applications.

EXPERIMENTAL SECTION

Analytical grade chemicals were used for synthesis without further purifications. Fluorine-doped tin oxide (FTO) conducting glass substrates, acquired from *Asahi Glass Company, Japan*, were cleaned by successive sonication with soap water, acetone, ethanol and deionized (DI) water for 15 min each with adequate drying prior to their use. Synthesis of ZnO nanorods (NRs) and sensitization of ZnO/TiO_2 nanoparticles (NPs) with porphyrins and metalloporphyrins are reported in previous publications.[40,68,72,85]

Characterization methods: Transmission electron microscopy (TEM) grids were prepared by applying a diluted drop of the TiO_2 samples to carbon-coated copper grids. Particle sizes were determined from micrographs recorded at a magnification of 100000X using an FEI (Technai S-Twin, operating at 200 kV) instrument. For optical experiments, the steady-state absorption and emission were determined with a Shimadzu UV-2450 spectrophotometer and a Jobin Yvon Fluoromax-3 fluorimeter respectively. Picosecond-resolved spectroscopic studies were done using a commercial time correlated single photon counting (TCSPC) setup from Edinburgh Instruments (instrument response function (IRF=80 ps), excitation at 409 nm). The observed fluorescence transients were fitted by using a nonlinear least square fitting procedure to a function $(X(t) = \int_0^t E(t')R(t-t')dt')$ comprising of convolution of the IRF (E(t)) with a sum of exponentials $(R(t) = A + \sum_{i=1}^{N} B_i e^{-t/\tau_i})$ with pre-exponential factors (B_i), characteristic lifetimes (τ_i) and a background (A). Relative concentration in a multi-exponential decay is finally expressed as, $c_n = \frac{B_n}{\sum_{i=1}^{N} B_i} \times 100.$ The average lifetime (amplitude-weighted) of a multi-exponential decay is expressed as $\tau_{av} = \sum_{i=1}^{N} c_i \tau_i$. FTIR spectra were recorded on a JASCO FTIR-6300 spectrometer, using CaF_2 window. Raman scattering measurements were performed by using a LabRAM HR, JobinY von fitted with a Peltier-cooled charge-coupled device (CCD) detector. An air cooled argon ion laser with a wavelength of 488 nm was used as the excitation light source. XPS measurements were carried out using XPS instrument (Omicron Nanotechnology) with Al K (1486.6 eV). The binding energies of the resultant XPS graphs were calibrated with respect to the C 1s feature at 284.6 eV. The spectra were deconvoluted to the individual components following Gaussian-Lorentzian function in Casa XPS software. Electrochemical experiments were performed using a CH analyser potentiostat (CHI1110C). For cyclic voltammetry, a three electrode system consisting of a platinum working electrode, a platinum counter electrode and a reference electrode was employed. All the potentials reported in this paper are referenced to the Ag/Ag^+ couple.

Femtosecond-resolved transient absorption study: In this study, Helios UV-NIR femtosecond transient absorption spectroscopy system was employed to measure transients of the samples.[86] Helios is equipped with CMOS VIS and InGaAs NIR spectrometers covering the range of 350-800 nm with 1.5 nm resolution at 9500 spectra/s and range of 800-1600 nm with 3.5 nm resolution at 7900 spectra/s, respectively. The probe beam is provided by Spectra-Physics Spitfire Pro 35F-XP regenerative femtosecond amplifier which produces 35fs pulses at 800 nm with 4 mJ of energy per pulse. A small portion (≈ 60 μJ) of the Spitfire output is routed via a delay line, adjustable pinholes, focusing lens, and variable neutral density filter to a crystal for white light continuum (WLC) generation; and further to the sample via a focusing mirror. Two crystals are available to cover Vis and NIR ranges. A computer controlled delay line is used to vary the delay between the pump and probe pulses that allow transient absorption measurements within a 3.3 ns time window. 1 mJ of the Spitfire output is used to pump TOPAS-C two stage parametric amplifier equipped with frequency mixing stages and non-collinear difference frequency generator that allows tuning from 240 to 2600 nm. TOPAS-C output beam is routed via adjustable pinholes, variable neutral density filter, depolarizer, chopper wheel and focusing lens to excite the sample. Pump and probe beams are overlapping spatially and temporally in the sample. Probe beam is collected by the spectrometer via collimating and focusing lenses, and wave pass filters to attenuate the white light around the Spitfire fundamental at 800 nm. All transient absorption experiments were conducted at room temperature. The observed transients were fitted using nonlinear least-squares fitting procedure (software SCIENTIST) to a function composed of the convolution of the instrument response function with a sum of exponentials. The purpose of this fitting is to obtain the decays in an analytic form suitable for further data analysis.

Materials and methods for the VLP process: For the photocatalysis study, ZnO NRs were grown on glass substrates using microwave irradiation (2.45 GHz) in a commercial microwave oven operated at low mode. Higher photocatalytic activity of the ZnO NRs grown by microwave assisted hydrothermal process have been previously reported.[87] A ZnO nanoparticle seed layer was initially deposited on glass substrates. Under the microwave irradiation, ZnO NRs were grown for 4 h using 20 mM aqueous solution of zinc nitrate and hexamethylenetetramine. As obtained NRs were then rinsed with DI water several times and annealed at 250 ^oC in air for 1 h. The sensitization of HP was carried out at room temperature.

A 5 μM aqueous solution of MB was then prepared in DI water which was used as the test contaminant for the photocatalysis test. A homemade flow-device consisting of two glass plates separated by a spacer was used to study the photocatalytic degradation of MB; in which, one of the glass plates of the symmetric device contained the ZnO NRs sensitized with HP dyes. The as prepared

MB solution was then injected through the flow-device and the device placed under a 500 W tungsten-halogen lamp, which was used as the visible light source in our study. The light was allowed to fall directly on the glass plate fabricated with HP-ZnO LHNs and in order to avoid the heat from the light source a 20 cm thick water bath was placed in between the light source and the flow-device. The position of the device was then adjusted to receive an incoming light power of 75 mW/cm^2. After 30 min of continuous light irradiation, the photoproduct was collected from the flow-device and its optical absorption spectrum was recorded to determine the percentage degradation (% DE) of MB using equation 8:

$$\%\,\mathrm{DE} = \frac{I_o - I}{I_o} \times 100 \qquad (8)$$

where, I_0 is the initial absorption intensity of MB at λ_{max}= 664 nm and I is the absorption intensity after 30 min of continuous photoirradiation.

The VLP process on MB in inert atmosphere was conducted in the similar way as described in the previous section using ZnO NRs sensitized with HP (24 h) as the catalyst media. Prior to the photocatalysis, argon (Ar) gas was passed through the MB solution for 30 min. Similarly, Ar gas was also passed through the flow-device for 30 min before injecting aqueous solution of MB. Finally, the solution was injected into the flow-device and photocatalysis was conducted for 30 min at light intensity of 75 mW/cm^2. During the photocatalysis, Ar gas was purged through the flow-device. After 30 minutes, the degraded product from the flow-device was collected and its optical absorption was measured to determine the percentage degradation of MB in inert atmosphere using equation 8.

In order to investigate the effect of metal ions presence as impurities in water, the home-made flow-device, in which one of the glass plates of the symmetric device contained the ZnO NPs sensitized with PP dyes. As prepared MB solution in DI water containing 0.07 mM Fe^{3+} and another with 0.07 mM Cu^{2+} were then injected through the flow-device and the device placed under the visible-light source in our study. The light was allowed to fall directly on the glass plate fabricated with PPIX−ZnO nanohybrids. The percentage degradation (%DE) of MB was determined using equation 8.

ACKNOWLEDGEMENTS

P.K. thanks the CSIR, India for fellowships. We thank DST (India) for financial grants DST/TM/SERI/2k11/103 and SB/S1/PC-011/2013. We also thank DAE (India) for financial grant, 2013/37P/73/BRNS. We would like to thank our colleagues and collaborators whose contributions over the years, acknowledged in the references, have been priceless in the successful evolution of the work in this area. In particular, we thank Dr. Soumik Sarkar, Dr. Abhinandan Makhal, Dr. Tanujjal Bora, Mr. Karthik Lakhsman, Mr. Myo Tay Zar Myint, Dr. Salim Al-Harthi, Dr. Achintya Singha, Dr. Omar F. Mohammed and Prof. Joydeep Dutta.

REFERENCES

1. K. Sauer. A role for manganese in oxygen evolution in photosynthesis. *Acc. Chem. Res.* **1980**, 13, 249-56.
2. K.S. Suslick, R.A. Watson. The photochemistry of chromium, manganese and iron porphyrin complexes. *New J. Chem.* **1992**, 16, 633-42.
3. A. Maldotti, R. Amadelli, C. Bartocci, V. Carassiti, E. Polo, G. Varani. Photochemistry of Iron-porphyrin complexes. Biomimetics and catalysis. *Coord. Chem. Rev.* **1993**, 125, 143-54.
4. W.D. Edwards, B. Weiner, M.C. Zerner. Electronic structure and spectra of various spin states of (porphinato)iron(III) chloride. *J. Phys. Chem.* **1988**, 92, 6188-97.
5. Y. Ozaki, K. Iriyama, H. Ogoshi, T. Kitagawa. Ligand-aided photoreduction of iron-porphyrin complexes probed by resonance Raman spectroscopy. *J. Am. Chem. Soc.* **1987**, 109, 5583-86.
6. C. Bartocci, F. Scandola, A. Ferri, V. Carassiti. Photoreduction of hemin in alcohol-containing mixed solvents. *J. Am. Chem. Soc.* **1980**, 102, 7067-72.
7. J.-M. Lehn. Supramolecular Chemistry—Scope and Perspectives Molecules, Supermolecules, and Molecular Devices (Nobel Lecture). *Angew. Chem. Int. Ed.* **1988**, 27, 89-112.
8. L. Que, W.B. Tolman. Biologically inspired oxidation catalysis. *Nature* **2008**, 455, 333-40.
9. D. Astruc. Electron-transfer processes in dendrimers and their implication in biology, catalysis, sensing and nanotechnology. *Nat. Chem.* **2012**, 4, 255-67.
10. O. Legrini, E. Oliveros, A.M. Braun. Photochemical processes for water treatment. *Chem. Rev.* **1993**, 93, 671-98.
11. M.A. Fox, M.T. Dulay. Heterogeneous photocatalysis. *Chem. Rev.* **1993**, 93, 341-57.
12. M.R. Hoffmann, S.T. Martin, W. Choi, D.W. Bahnemann. Environmental Applications of Semiconductor Photocatalysis. *Chem. Rev.* **1995**, 95, 69-96.
13. C.C. Chen, X.Z. Li, W.H. Ma, J.C. Zhao, H. Hidaka, N. Serpone. Effect of transition metal ions on the TiO_2 -assisted photo-degradation of dyes under visible irradiation: A probe for the interfacial electron transfer process and reaction mechanism. *J. Phys. Chem. B* **2002**, 106, 318-24.
14. R. Asahi, T. Morikawa, T. Ohwaki, K. Aoki, Y. Taga. Visible-light photocatalysis in nitrogen-doped titanium oxides. *Science* **2001**, 293, 269-71.
15. N. Lu, X. Quan, J. Li, S. Chen, H. Yu, G. Chen. Fabrication of boron-doped TiO_2 nanotube array electrode and investigation of its photoelectrochemical capability. *J. Phys. Chem. C* **2007**, 111, 11836-42.
16. X.Z. Li, F.B. Li. Study of Au/Au 3+ -TiO 2 Photocatalysts toward visible photooxidation for water and wastewater treatment. *Environ. Sci. Technol.* **2001**, 35, 2381-87.
17. Z. Zhang, W. Wang, L. Wang, S. Sun. Enhancement of Visible-Light Photocatalysis by Coupling with Narrow-Band-Gap Semiconductor: A Case Study on Bi_2S_3/Bi_2WO_6. *ACS Appl. Mater. Interfaces* **2012**, 4, 593−97.
18. J. Jiang, X. Zhang, P. Sun, L. Zhang. ZnO/BiOI Heterostructures: Photoinduced Charge-Transfer Property and Enhanced Visible-Light Photocatalytic Activity. *J. Phys. Chem. C* **2011**, 115, 20555-64.
19. G.S. Li, D.Q. Zhang, J.C. Yu. A new visible-light photocatalyst: CdS quantum dots embedded mesoporous TiO_2. *Environ. Sci. Technol.* **2009**, 43, 7079-85.
20. H. Zhang, R.L. Zong, J.C. Zhao, Y.F. Zhu. Dramatic visible photocatalytic degradation performances due to synergetic effect of TiO_2 with PANI. *Environ. Sci. Technol.* **2008**, 42, 3803-07.
21. W. Zhao, Y. Sun, F.N. Castellano. Visible-Light Induced Water Detoxification Catalyzed by Pt II Dye Sensitized Titania. *J. Am. Chem. Soc.* **2008**, 130, 12566-67.
22. Q. Sun, Y. Xu. Sensitization of TiO_2 with Aluminum Phthalocyanine: Factors Influencing the Efficiency for Chlorophenol Degradation in Water under Visible Light. *J. Phys. Chem. C* **2009**, 113, 12387-94.
23. E. Bae, W. Choi. Highly Enhanced Photoreductive Degradation of Perchlorinated Compounds on Dye-Sensitized Metal/TiO_2 under Visible Light. *Environ. Sci. Technol.* **2003**, 37, 147-52.
24. B. Oregan, M. Gratzel. A low-cost, high-efficiency solar-cell based on dye-sensitized colloidal TiO_2 films. *Nature* **1991**, 353, 737-40.
25. A. Fujishima, K. Honda. Electrochemical photolysis of water at a semiconductor electrode. *Nature* **1972**, 238, 37-38.
26. H. Zhou, T. Fan, D. Zhang. Biotemplated Materials for Sustainable Energy and Environment: Current Status and Challenges. *ChemSusChem* **2011**, 4, 1344-87.
27. Y. Sun, Q. Wu, G. Shi. Graphene based new energy materials. *Energy Environ. Sci.* **2011**, 4, 1113-32.
28. L.M. Peter. The Grätzel Cell : Where Next? *J. Phys. Chem. Lett.* **2011**, 2, 1861-67.

29. J.N. Demas, D. Diemente, E.W. Harris. Oxygen quenching of charge-transfer excited states of ruthenium(II) complexes. Evidence for singlet oxygen production. *J. Am. Chem. Soc.* **1973**, 95, 6864-65.
30. S.L. Buell, J.N. Demas. Heterogeneous preparation of singlet oxygen using an ion-exchange-resin-bound tris(2,2'-bipyridine)ruthenium(II) photosensitizer. *J. Phys. Chem.* **1983**, 87, 4675-81.
31. J.W. Dobrucki. Interaction of oxygen-sensitive luminescent probes Ru(phen)32+ and Ru(bipy)32+ with animal and plant cells in vitro: Mechanism of phototoxicity and conditions for non-invasive oxygen measurements. *J. Photochem. Photobiol. B* **2001**, 65, 136-44.
32. N. Robertson. Optimizing Dyes for Dye-Sensitized Solar Cells. *Angew. Chem. Int. Ed.* **2006**, 45, 2338-45.
33. H. Hayashi, I.V. Lightcap, M. Tsujimoto, M. Takano, T. Umeyama, P.V. Kamat, H. Imahori. Electron Transfer Cascade by Organic/Inorganic Ternary Composites of Porphyrin, Zinc Oxide Nanoparticles, and Reduced Graphene Oxide on a Tin Oxide Electrode that Exhibits Efficient Photocurrent Generation. *J. Am. Chem. Soc.* **2011**, 133, 7684-87.
34. A. Yella, H.-W. Lee, H.N. Tsao, C. Yi, A.K. Chandiran, M.K. Nazeeruddin, E.W.-G. Diau, C.-Y. Yeh*et. al*. Porphyrin-Sensitized Solar Cells with Cobalt (II/III)–Based Redox Electrolyte Exceed 12 Percent Efficiency. *Science* **2011**, 334, 629-34.
35. L.-L. Li, E.W.-G. Diau. Porphyrin-sensitized solar cells. *Chem. Soc. Rev.* **2013**, 42, 291-304.
36. M.-y. Duan, J. Li, G. Mele, C. Wang, X.-f. Lü, G. Vasapollo, F.-x. Zhang. Photocatalytic Activity of Novel Tin Porphyrin/TiO_2 Based Composites. *J. Phys. Chem. C* **2010**, 114, 7857-62.
37. E.A. Lissi, M.V. Encinas, E. Lemp, M.A. Rubio. Singlet oxygen O2(1.DELTA.g) bimolecular processes. Solvent and compartmentalization effects. *Chem. Rev.* **1993**, 93, 699-723.
38. M.J. Griffith, K. Sunahara, P. Wagner, K. Wagner, G.G. Wallace, D.L. Officer, A. Furube, R. Katoh*et. al*. Porphyrins for dye-sensitised solar cells: new insights into efficiency-determining electron transfer steps. *Chem. Commun.* **2012**, 48, 4145-62.
39. T. Bessho, S.M. Zakeeruddin, C.-Y. Yeh, E.W.-G. Diau, M. Grätzel. Highly Efficient Mesoscopic Dye-Sensitized Solar Cells Based on Donor–Acceptor-Substituted Porphyrins. *Angew. Chem.* **2010**, 122, 6796-99.
40. S. Sarkar, A. Makhal, T. Bora, K. Lakhsman, A. Singha, J. Dutta, S.K. Pal. Hematoporphyrin–ZnO Nanohybrids: Twin Applications in Efficient Visible-Light Photocatalysis and Dye-Sensitized Solar Cells. *ACS Appl. Mater. Interfaces* **2012**, 4, 7027-35.
41. N. Masi Reddy, T.-Y. Pan, Y. Christu Rajan, B.-C. Guo, C.-M. Lan, E. Wei-Guang Diau, C.-Y. Yeh. Porphyrin sensitizers with [small pi]-extended pull units for dye-sensitized solar cells. *Phys. Chem. Chem. Phys.* **2013**, 15, 8409-15.
42. T. Hasobe. Supramolecular nanoarchitectures for light energy conversion. *Phys. Chem. Chem. Phys.* **2010**, 12, 44-57.
43. S. Rodrigues, K.T. Ranjit, S. Uma, I.N. Martyanov, K.J. Klabunde. Single-Step Synthesis of a Highly Active Visible-Light Photocatalyst for Oxidation of a Common Indoor Air Pollutant: Acetaldehyde. *Adv. Mater.* **2005**, 17, 2467-71.
44. A.A. Ismail, D.W. Bahnemann. Metal-Free Porphyrin-Sensitized Mesoporous Titania Films For Visible-Light Indoor Air Oxidation. *ChemSusChem* **2010**, 3, 1057-62.
45. D. Li, W. Dong, S. Sun, Z. Shi, S. Feng. Photocatalytic Degradation of Acid Chrome Blue K with Porphyrin-Sensitized TiO_2 under Visible Light. *J. Phys. Chem. C* **2008**, 112, 14878-82.
46. H. Huang, X. Gu, J. Zhou, K. Ji, H. Liu, Y. Feng. Photocatalytic degradation of Rhodamine B on TiO_2 nanoparticles modified with porphyrin and iron-porphyrin. *Catal. Commun.* **2009**, 11, 58-61.
47. G. Granados-Oliveros, E.A. Páez-Mozo, F.M. Ortega, C. Ferronato, J.-M. Chovelon. Degradation of atrazine using metalloporphyrins supported on TiO_2 under visible light irradiation. *Appl. Catal., B* **2009**, 89, 448-54.
48. T. Shiragami, J. Matsumoto, H. Inoue, M. Yasuda. Antimony porphyrin complexes as visible-light driven photocatalyst. *J. Photochem. Photobiol. C* **2005**, 6, 227-48.
49. A. Maldotti, L. Andreotti, A. Molinari, V. Carassiti. Photochemically driven models of oxygenases based on the use of iron porphyrins. *J. Biol. Inorg. Chem.* **1999**, 4, 154-61.
50. D. Ricard, M. L'Her, P. Richard, B. Boitrel. Iron Porphyrins as Models of Cytochrome c Oxidase. *Chem. Eur. J.* **2001**, 7, 3291-97.
51. N. Hessenauer-Ilicheva, A. Franke, D. Meyer, W.-D. Woggon, R. van Eldik. Mechanistic Insight into Formation of Oxo-Iron(IV) Porphyrin π-Cation Radicals from Enzyme Mimics of Cytochrome P450 in Organic Solvents. *Chem. Eur. J.* **2009**, 15, 2941-59.
52. Y. Shen, U. Ryde. Reaction Mechanism of Porphyrin Metallation Studied by Theoretical Methods. *Chem. Eur. J.* **2005**, 11, 1549-64.
53. M. Inamo, N. Kamiya, Y. Inada, M. Nomura, S. Funahashi. Structural Characterization and Formation Kinetics of Sitting-Atop (SAT) Complexes of Some Porphyrins with Copper(II) Ion in Aqueous Acetonitrile Relevant to Porphyrin Metalation Mechanism. Structures of Aquacopper(II) and Cu(II)−SAT Complexes As Determined by XAFS Spectroscopy. *Inorg. Chem.* **2001**, 40, 5636-44.
54. S. Funahashi, Y. Inada, M. Inamo. Dynamic Study of Metal-Ion Incorporation into Porphyrins Based on the Dynamic Characterization of Metal Ions and on Sitting-Atop Complex Formation. *Anal. Sci.* **2001**, 17, 917-27.
55. H.Z. Yu, J.S. Baskin, B. Steiger, C.Z. Wan, F.C. Anson, A.H. Zewail. Femtosecond dynamics of metalloporphyrins: electron transfer and energy redistribution. *Chem. Phys. Lett.* **1998**, 293, 1-8.
56. C. Wang, J. Li, G. Mele, G.-M. Yang, F.-X. Zhang, L. Palmisano, G. Vasapollo. Efficient degradation of 4-nitrophenol by using functionalized porphyrin-TiO2 photocatalysts under visible irradiation. *Appl. Catal., B* **2007**, 76, 218-26.
57. N. Nasuha, B.H. Hameed, A.T.M. Din. Rejected tea as a potential low-cost adsorbent for the removal of methylene blue. *J. Hazard. Mater.* **2010**, 175, 126-32.
58. R.C. Srivastava, V.D. Anand, W.R. Carper. A Fluorescence Study of Hematoporphyrin. *Appl. Spectroscopy* **1973**, 27, 444-49.
59. P. Castillero, J.R. Sanchez-Valencia, M. Cano, J.M. Pedrosa, J. Roales, A. Barranco, A.R. Gonzalez-Elipe. Active and Optically Transparent Tetracationic Porphyrin/TiO_2 Composite Thin Films. *ACS Appl. Mater. Interfaces.* **2010**, 2, 712–21.
60. W. Tu, J. Lei, P. Wang, H. Ju. Photoelectrochemistry of Free-Base-Porphyrin-Functionalized Zinc Oxide Nanoparticles and Their Applications in Biosensing. *Chem. Eur. J.* **2011**, 17, 9440 - 47.
61. T. Hasobe, K. Saito, P.V. Kamat, V. Troiani, H. Qui, N. Solladie, K.S. Kim, J.K. Park*et. al*. *J. Mater. Chem.* **2007**, 17, 4160-70.
62. H. Saarenpaa, E. Sariola-Leikas, A.P. Perros, J.M. Kontio, A. Efimov, H. Hayashi, H. Lipsanen, H. Imahori*et. al*. Self-Assembled Porphyrins on Modified Zinc Oxide Nanorods: Development of Model Systems for Inorganic−Organic Semiconductor Interface Studies. *J. Phys. Chem. C* **2012**, 116, 2336−43.
63. H.M. Cheng, W.F. Hsieh. Electron transfer properties of organic dye-sensitized solar cells based on indoline sensitizers with ZnO nanoparticles. *Nanotechnology* **2010**, 21, 485202.
64. G.B. Deacon, R.J. Phillips. Relationships between the carbon-oxygen stretching frequencies of carboxylato complexes and the type of carboxylate coordination. *Coord. Chem. Rev.* **1980**, 33, 227-50.
65. Y. Zhang, H. Jia, R. Wang, C. Chen, X. Luo, D. Yu, C. Lee. Low-temperature growth and Raman scattering study of vertically aligned ZnO nanowires on Si substrate. *Appl. Phys. Lett.* **2003**, 83, 4631-33.
66. P. Jiang, J.J. Zhou, H.F. Fang, C.Y. Wang, Z.L. Wang, S.S. Xie. *Adv. Funct. Mater.* **2007**, 17, 1303.
67. S. Sarkar, A. Makhal, K. Lakshman, T. Bora, J. Dutta, S.K. Pal. "Dual-Sensitization" via Electron and Energy Harvesting in CdTe Quantum Dots Decorated ZnO Nanorod-based Dye-Sensitized Solar Cells. *J. Phys. Chem. C* **2012**, 116, 14248−56.
68. S. Sardar, S. Sarkar, M.T.Z. Myint, S. Al-Harthi, J. Dutta, S.K. Pal. Role of central metal ions in hematoporphyrin-functionalized titania in solar energy conversion dynamics. *Phys. Chem. Chem. Phys.* **2013**, 15, 18562-70.
69. V. Shklover, M.K. Nazeeruddin, S.M. Zakeeruddin, C. Barbé, A. Kay, T. Haibach, W. Steurer, R. Hermann*et. al*. Structure of Nanocrystalline TiO_2 Powders and Precursor to Their Highly Efficient Photosensitizer. *Chem. Mater.* **1997**, 9, 430-39.
70. H.C. Choi, Y.M. Jung, S.B. Kim. Size effects in the Raman spectra of TiO_2 nanoparticles. *Vib. Spectrosc* **2005**, 37, 33-38.
71. S. Franzen, L. Kiger, C. Poyart, J.-L. Martin. Heme Photolysis Occurs by Ultrafast Excited State Metal-to-Ring Charge Transfer. *Biophys. J* . **2001**, 80, 2372-85.
72. P. Kar, S. Sardar, E. Alarousu, J. Sun, Z.S. Seddigi, S.A. Ahmed, E.Y. Danish, O.F. Mohammed, S.K. Pal. Impact of Metal Ions in Porphyrin-Based Applied Materials for Visible-Light Photocatalysis: Key Information from Ultrafast Electronic Spectroscopy. *Chem. Eur. J.* **2014**, DOI: 10.1002/chem.201402632.
73. S. Fujihara, H. Naito, T. Kimura. Visible photoluminescence of ZnO nanoparticles dispersed in highly transparent MgF2 thin-films via sol–gel process. *Thin Solid Films* **2001**, 389, 227-32.

74. E. Collini, C. Ferrante, R. Bozio. Strong Enhancement of the Two-Photon Absorption of Tetrakis(4-sulfonatophenyl)porphyrin Diacid in Water upon Aggregation. *J. Phys. Chem. B* **2004**, 109, 2-5.
75. S. Verma, A. Ghosh, A. Das, H.N. Ghosh. Ultrafast Exciton Dynamics of J- and H-Aggregates of the Porphyrin-Catechol in Aqueous Solution. *J. Phys. Chem. B* **2010**, 114, 8327-34.
76. G. Mele, R. Sole, G. Vasapollo, E. García-López, L. Palmisano, L. Jun, R. Słota, G. Dyrda. TiO2-based photocatalysts impregnated with metallo-porphyrins employed for degradation of 4-nitrophenol in aqueous solutions: role of metal and macrocycle. *Res. Chem. Intermed.* **2007**, 33, 433-48.
77. S.G. Kruglik, P.A. Apanasevich, V.S. Chirvony, V.V. Kvach, V.A. Orlovich. Resonance Raman, CARS, and Picosecond Absorption Spectroscopy of Copper Porphyrins: The Evidence for the Exciplex Formation with Oxygen-Containing Solvent Molecules. *J. Phys. Chem.* **1995**, 99, 2978-95.
78. D. Kim, D. Holten, M. Gouterman. Evidence from picosecond transient absorption and kinetic studies of charge-transfer states in copper(II) porphyrins. *J. Am. Chem. Soc.* **1984**, 106, 2793-98.
79. S. Sarkar, A. Makhal, S. Baruah, M.A. Mahmood, J. Dutta, S.K. Pal. Nanoparticle-Sensitized Photodegradation of Bilirubin and Potential Therapeutic Application. *J. Phys. Chem. C* **2012**, 116, 9608-15.
80. S. Afzal, W.A. Daoud, S.J. Langford. Photostable Self-Cleaning Cotton by a Copper(II) Porphyrin/TiO2 Visible-Light Photocatalytic System. *ACS Appl. Mater. Interfaces* **2013**, 5, 4753-59.
81. E.B. Fleischer, E.I. Choi, P. Hambright, A. Stone. Porphyrin Studies: Kinetics of Metalloporphyrin Formation. *Inorg Chem* **1964**, 3, 1284-87.
82. P. Castillero, J.R. Sánchez-Valencia, M. Cano, J.M. Pedrosa, J. Roales, A. Barranco, A.n.R. González-Elipe. Active and Optically Transparent Tetracationic Porphyrin/TiO_2 Composite Thin Films. *ACS Appl. Mater. Interfaces* **2010**, 2, 712-21.
83. A. Kongkanand, K. Tvrdy, K. Takechi, M. Kuno, P.V. Kamat. Quantum Dot Solar Cells. Tuning Photoresponse through Size and Shape Control of CdSe−TiO_2 Architecture. *J. Am. Chem. Soc.* **2008**, 130, 4007-15.
84. A. Kathiravan, P.S. Kumar, R. Renganathan, S. Anandan. Photoinduced electron transfer reactions between meso-tetrakis(4-sulfonatophenyl)porphyrin and colloidal metal-semiconductor nanoparticles. *Colloids Surf., A* **2009**, 333, 175-81.
85. S. Sarkar, A. Makhal, K. Lakshman, T. Bora, J. Dutta, S.K. Pal. Dual-Sensitization via Electron and Energy Harvesting in CdTe Quantum Dots Decorated ZnO Nanorod-Based Dye-Sensitized Solar Cells. *J. Phys. Chem. C* **2012**, 116, 14248-56.
86. J. Sun, W. Yu, A. Usman, T.T. Isimjan, S. Dgobbo, E. Alarousu, K. Takanabe, O.F. Mohammed. Generation of Multiple Excitons in Ag2S Quantum Dots: Single High-Energy versus Multiple-Photon Excitation. *J. Phys. Chem. Lett.* **2014**, 5, 659-65.
87. S. Baruah, M.A. Mahmood, M.T.Z. Myint, T. Bora, J. Dutta. *Beilstein J. Nanotechnol.* **2010**, 1, 14-20.